Measuring Matter in a Tight Spot:
A Novel Approach for Characterizing Ultra-Thin Films and Confined Fluids

By

DANIEL FOREST KIENLE
B.S. (University of Colorado, Boulder) 2011
M.S. (University of Colorado, Boulder) 2011
DISSERTATION

Submitted in partial satisfaction of the requirements for the degree of

DOCTOR OF PHILOSOPHY

In

Chemical Engineering
in the
OFFICE OF GRADUATE STUDIES
of the
UNIVERSITY OF CALIFORNIA
DAVIS

Approved:

_____

Tonya L. Kuhl, Chair

_____

Stephanie R. Dungan

_____

Atul N. Parikh

Committee in Charge

2016

i

ProQuest Number: 10190858

ProQuest 10190858

Contents

Abstract

The behavior of matter confined to molecular dimensions is technologically relevant as device size decreases but fundamentally vexing as continuum theory breaks down and the role of molecular size and configuration become important. Due to the extremely small dimensions, studying properties of confined matter is difficult, typically requiring very specialized techniques such as x-ray or neutron scattering. In this work, analysis of multiple beam interferometry (MBI) was advanced to enable characterization of the optical properties of ultrathin solid and liquid films. In the first part of the work, conventional MBI contact analysis was used to determine the thickness and refractive index of previously uncharacterized lipid monolayers commonly used in biological membrane research, and results demonstrated that the inner and outer leaflet of supported lipid bilayers have different optical properties. MBI analysis was then extended to allow the optical thickness of thin films to be measured without film contact and free from systematic error through design of a novel analytical approach called the refractive index profile correction (RIPC) method. This development enabled soft condensed matter samples which are frequently fragile, reactive, or easily deformable films to be characterized without compressing or contacting the films. Importantly, properties of interfacial films at the surface, such as concentration gradients due to absorbed layers or depletion layers, can be directly measured as a function of confinement and compared to their properties in the bulk using this newly developed approach. Furthermore, the technique is applicable to complex interferometer samples which may include: (1) interferometers with substrates of non-uniform thickness leading to asymmetry of the sample; or (2) systems with an additional layer between the substrate and the film of interest wherein, all properties can be accurately determined without independent measurements or *a priori* knowledge of any layer properties. Thus, the technique is applicable to a diverse array of systems, through the ability to tailor the chemistry of the confining surfaces and determine interaction forces while simultaneously

determining the refractive index and thereby concentration of the confined materials. The method was applied to take non-contact measurements of the mass of polyelectrolyte brushes adsorbed on mica from water, and demonstrated that the mass of the polymer film was conserved during confinement and compression. The method was also used to independently characterize both the effects that a single surface has on fluid structure and the effects that confinement has on the fluid structure using the non-polar fluid octamethylcylclotetrasiloxane (OMCTS). The results present a conclusive demonstration that there is no first-order phase transition or any resolvable deviation from the bulk fluid density during confinement, thereby answering a fundamental question as to the state of confined liquids.

Chapter I

Thickness and Refractive Index of DPPC and DPPE Monolayers by Multiple-Beam Interferometry

Daniel F. Kienle,[†] João V. de Souza,[‡] Erik B. Watkins,[§] and Tonya L. Kuhl[†]*

[†]Department of Chemical Engineering and Materials Science, University of California Davis, 95616, USA
[‡]Department of Chemistry, University of California Davis, 95616, USA
[§]Biophysics Graduate Group, University of California, Davis, 95616, USA;
Large Scale Structures (LSS) Group, Institut Laue-Langevin, Grenoble, France

Abstract

The thickness and refractive index of 1,2-Dipalmitoyl-sn-glycero-3-phosphocholine (DPPC) and 1,2-Dipalmitoyl-sn-glycero-3-phosphoethanolamine (DPPE) monolayers Langmuir-Blodgett (LB) deposited on mica were measured in dry air and bulk water using multiple beam interferometry (MBI). Measurements of thickness using atomic force microscopy (AFM) of identical monolayers (AFM measurements and AFM experimental procedure done by João V. de Souza), and X-ray reflectivity (XRR) of the monolayers on quartz (XRR measurements were performed by Erik B. Watkins, and detailed XRR experimental procedure, analysis details, and results were written by Erik B. Watkins and Tonya L. Kuhl) were taken for comparison. The measurement of the properties of solid-supported monolayers in dry air allows lipid optical properties to be determined free from solvent effects. The thickness and refractive index measured by MBI, respectively were 25.5 ± 0.6 Å and 1.485 ± 0.007 for DPPE monolayers, and 23.9 ± 0.5 Å and 1.478 ± 0.006 for DPPC monolayers in dry air. These thicknesses are consistent with the other techniques used in this work as well as other measurements in the literature. The refractive indices of solid-supported lipid monolayers have not been previously measured. The values are higher than

previous measurements on black lipid films done by reflectometry, which is attributed to increased lipid packing density and the absence of hydrocarbon solvents. Applying water to the monolayers had no measurable effect on their properties, indicating that any change in hydration is below detection.

Introduction

Solid supported lipid bilayers (SLB) of DPPC and DPPE are an especially useful model for cell membranes because they are stable over long periods of time, and the use of a solid planar support opens the door to a number of powerful characterization techniques [1]. There have been many studies on the structure of solid-supported monolayers [2-5], but none have been devoted to measuring their optical properties, which are not only useful for probing structural characteristic of the monolayer, but are also required for many techniques used to study SLBs. Measurement of lipid monolayer properties at the air-solid interface can return the properties of pure oriented lipid, whereas measurement at a liquid interface will include the effects of hydration and protrusions of the lipids [6, 7].

The majority of techniques that have been used to characterize thin biological films require assumptions about the film properties. In particular, experiments have been done using ellipsometry [4, 8, 9], surface plasmon resonance [10] , Brewster angle microscopy [11], impedance analysis [12], which all require a known refractive index or dielectric properties. In the case of solid-supported lipid monolayers, the refractive index has never been measured and values measured for bulk lipids or lipid in different forms or geometries are instead used; inaccuracies due to the differences in packing density between oriented systems or the birefringence exhibited by lipids when they form an oriented monolayer or bilayer [13-15] can result in incorrect determination of subsequent properties.

Other techniques that do not require a known refractive index have been very effective in returning the properties of thin biological films, and have been more frequently applied to phospholipid monolayers than other techniques. X-ray, neutron and electron scattering [2, 7, 16-19] and AFM [3, 5, 9,

2

20, 21] experiments have been used to obtain detailed structural and topographical properties of lipid monolayers and bilayers with very high resolution. The more recently developed optical techniques of coupled waveguide lightmode resonance (CWLR) spectroscopy [22] and optical waveguide lightmode spectroscopy (OWLS) [23] and dual polarization interferometry (DPI) [24] can independently measure the thickness and refractive index of thin films. All of these techniques are capable of measuring refractive index shifts in real time. CWLR and DPI can also measure the film birefringence in real time and CWLR can simultaneously determine film thickness as well [22, 25]. These techniques are profoundly useful for measuring the dynamics of protein-membrane interactions [14, 26-28] and membrane formation from vesicle fusion [25, 29, 30]. Unfortunately, these techniques have found no application to lipid monolayers at the solid-air interface, most likely because background measurements with just the substrate need to be taken in situ.

MBI is presented here as a compliment to CWLR, OWLS and DPI for measurements of thickness and refractive index and is applied to a supported lipid monolayer. While MBI is only capable of measuring birefringence in the plane of the surface [31] and would be impractical for measuring dynamics of thin films, it maintains the advantage of being less restricted in substrate materials and geometry and has been used with glass [32], metal films [33], and sapphire [34]. Currently we are experimenting with thin carbon surfaces. CWLR, OWLS and DPI all require substrates with specific optical and geometric properties. MBI simply requires the substrate to have one reflective surface, to be sufficiently transparent, and to be within a certain thickness range that depends on the instrumentation (typically 2-8 μ). Mica is particularly well suited for MBI studies as the basal plane cleavage can yield remarkably thin, atomically smooth sheets. However, mica's layered structure renders it generally unusable as a substrate in x-ray scattering, neutron scattering or any of the aforementioned optical techniques, although a recent XRR study has made use of mica as a substrate for thin film measurements [35].

It has been known for a long time that MBI is theoretically capable of this type of measurement using the surface force apparatus (SFA) [36], and the theory has been periodically reassessed since the instrument's invention [37-39].   However, the technique has only been used a few times for measurements of both refractive index and thickness of thin biological films [6, 36], and none of these measurements were taken on monolayers. Measurements on multilayers have the advantage of higher accuracy as the uncertainty is divided amongst the layers, but they do not isolate the properties of the individual monolayers which will be affected by hydration between head groups of adjacent monolayers. Bilayers are commonly studied using the SFA, but measurements have assumed properties based on estimated values or those found in the literature for similar lipids [6, 40].   Similar to other optical techniques, this is due to the challenge of measuring substrate properties in situ.   This obstacle is resolved by removing the lipid monolayer using UV-ozone treatment and rinsing with water, and then taking measurement on the mica substrate without altering the orientation of the samples or optics. This is necessary because even slightly altering the orientation of the sample can affect the apparent properties of the mica substrate. Similar methods have been employed in the past [40].

Using MBI, we have accurately measured the thickness and refractive index of mica-supported DPPC and DPPE monolayers, which are commonly used as stable inner leaflets for biological membrane experiments [6]. Measurements were taken in dry air and bulk water in an attempt to isolate the effects of monolayer-substrate hydration on the optical properties of supported lipids. We have also performed complementary measurements of the thicknesses using AFM and x-ray reflectivity (XRR), as well as compiled results from the literature for comparison. The results are used to discuss differences between solid-supported monolayers and other lipid systems.

Experimental

Materials

1,2-Dipalmitoyl-*sn*-glycero-3-phosphocholine (DPPC) and 1,2-Dipalmitoyl-*sn*-glycero-3-phosphoethanolamine (DPPE) were purchased from Avanti Polar Lipids, Inc. (Alabaster, AL). The lipids were dissolved in 9:1 chloroform:methanol solutions at concentrations of 1-2 mg/ml. All water used was purified with a Milli-Q gradient water purification system with a resistivity of 18 MΩ·cm.

Sample Preparation

Ruby muscovite mica was used as the substrate for both AFM and MBI measurements. For MBI measurements, the mica substrates were cleaved to thin sheets of uniform thickness. The sheets were adhered to a clean mica backing sheet and 55 nm of silver was vacuum deposited onto one side of the cleaved mica. Subsequently, a single silvered sheet of uniform thickness was divided and glued onto 2 cylindrical glass discs mica-side-out, using an epoxy resin, to create an optical interferometer. For AFM measurements, mica was cleaved and used immediately. For XRR, the substrate was single crystal quartz polished to a flatness of λ/10. Prior to use the quartz was carefully sonicated in Helmanex (Hellma Analytics), rinsed thoroughly with MilliQ water, dried, and then sonicated in acetone, then isopropanol, and rinsed with MilliQ water and dried in clean nitrogen. Finally, the quartz was cleaned with UV ozone for at least 30 minutes just prior to lipid deposition [41, 42]. In all cases, the DPPC and DPPE monolayers were prepared by Langmuir-Blodgett deposition using a Wilhelmy trough (Nima Coventry, U.K.) from pure water onto the mica or quartz substrates at 25 °C with a surface pressure of 45 mN/m.

Measurement Techniques

The AFM measurements taken in this study employed a MFP-3D-Bio Atomic Force Microscope and Silicon cantilevers, both from Asylum Research (Santa Barbara, CA). The spring constant of the cantilevers was 1.46 N/m. To scan the samples, a force of 0.14 nN was employed in contact mode, at a

10 μm/s scanning rate. A square depression in the DPPE monolayer was required to measure the thickness due to a lack of defects in the monolayer (see Figure 1.1). This was produced using a 1.7 nN force also in contact mode and was then imaged by scanning in the same region using the lower force.

X-ray reflectivity measurements were performed at beamline 6-ID at the Advanced Photon Source (Argonne National Laboratory, IL). The x-ray wavelength was 0.54 Å, and the measured wave vector transfer, q_z, range extended approximately from 0.02 to 0.5 Å^{-1}. Specular reflectivities, R, above noise level were obtained down to values of R = 10^{-8}. The experimental uncertainties were estimated by the photon counting statistics (standard deviation, σR) with the experimental resolution in q_z being approximated by Δq_z = 0.0003 Å^{-1} for the measured q_z range.

Thickness and refractive index were determined using MBI measurements taken on the deposited lipid monolayers on atomically smooth, back-silvered mica surfaces with a Mark II surface force apparatus (SFA). To do this, two mica sheets of the same thickness were first glued onto cylindrical, glass discs. After deposition of the lipid monolayer, the discs were mounted in the SFA in a cross cylindrical geometry where they formed an interferometer. Collimated white light from a tungsten halogen source was directed through the interferometer which results in intensity peaks at discrete wavelengths.

For the simplest, single layer interferometer, the intensity peaks occur at wavelengths that are a whole order multiple of the optical thickness ($\Omega = T \times n$, where T is the layer thickness and n is the layer refractive index) of the interferometer, because the light reflecting between the mirrors constructively interferes and is transmitted at high intensity. Light at wavelengths that are not a whole order multiple of the optical thickness destructively interfere and are transmitted at low intensity. The interference pattern of multilayer interferometers is more complicated due to the additional interfaces. These peaks are called fringes of equal chromatic order (FECO) and the wavelength at which they occur depends on the optical properties of the layers in the interferometer [36]. The FECO were separated using a spectrometer, and captured using a CCD camera (Princeton SPEC-10:2K Roper Scientific, Trenton NJ).

6

Measurements were first taken on the DPPE and DPPC monolayers after being sealed in the SFA with P_2O_5 for 1 hour to dry the air and prevent damaging condensation on the surfaces. The monolayer surfaces were brought into contact where the monolayers formed a bilayer of either DPPE or DPPC between the mica substrates, and spectra were taken. The monolayers were then removed from the mica surfaces by separating them and placing a UV pen lamp between the two surfaces (~1 mm from each) and illuminating them for a total of one hour which was broken into three 20 minutes increments with 10 minutes breaks to prevent temperature induced bubbles or deformation in the glue. Afterward the surfaces were rinsed with pure, room temperature water without wetting the glue, which becomes partially soluble during UV-ozone treatment. For several test surfaces, after removal of the monolayer, the contact angle of pure water was measured to be < 5°, indicating that the monolayer was fully removed from the mica support. The rinsing step consistently removed material from the mica surfaces illustrating its necessity for removing residual molecule fragments and ions. After removing the monolayer, the surfaces were allowed to reach room temperature and placed into contact where another spectrum was taken. The experiment was repeated with nine DPPE surfaces and ten DPPC surfaces. If either the refractive index or the thickness were identified as outliers according to Chauvenet's criterion, the data for both the refractive index and thickness of the sample were discarded. Seven measurements for each lipid monolayer remained after removal of the outliers.

For several samples of DPPC and DPPE, an additional measurement was taken after applying water to the monolayer surfaces while still in contact in an attempt to detect any changes in the hydration of the monolayer when going from dry air to bulk water. The water was sprayed onto the contacted surfaces using a syringe and allowed to equilibrate for ten minutes before measurements were taken.

Analysis and Results

Atomic Force Microscopy

The AFM images of DPPC and DPPE are shown in Figure 1.1a and b respectively. The DPPE monolayer showed no defects while DPPC had numerous small defects. These defects were used to determine the monolayer thickness of DPPC, while depression had to be carved into the monolayer of DPPE using the AFM probe to get a measure of the thickness. An image of one of the carved regions is shown in Figure 1.1c.
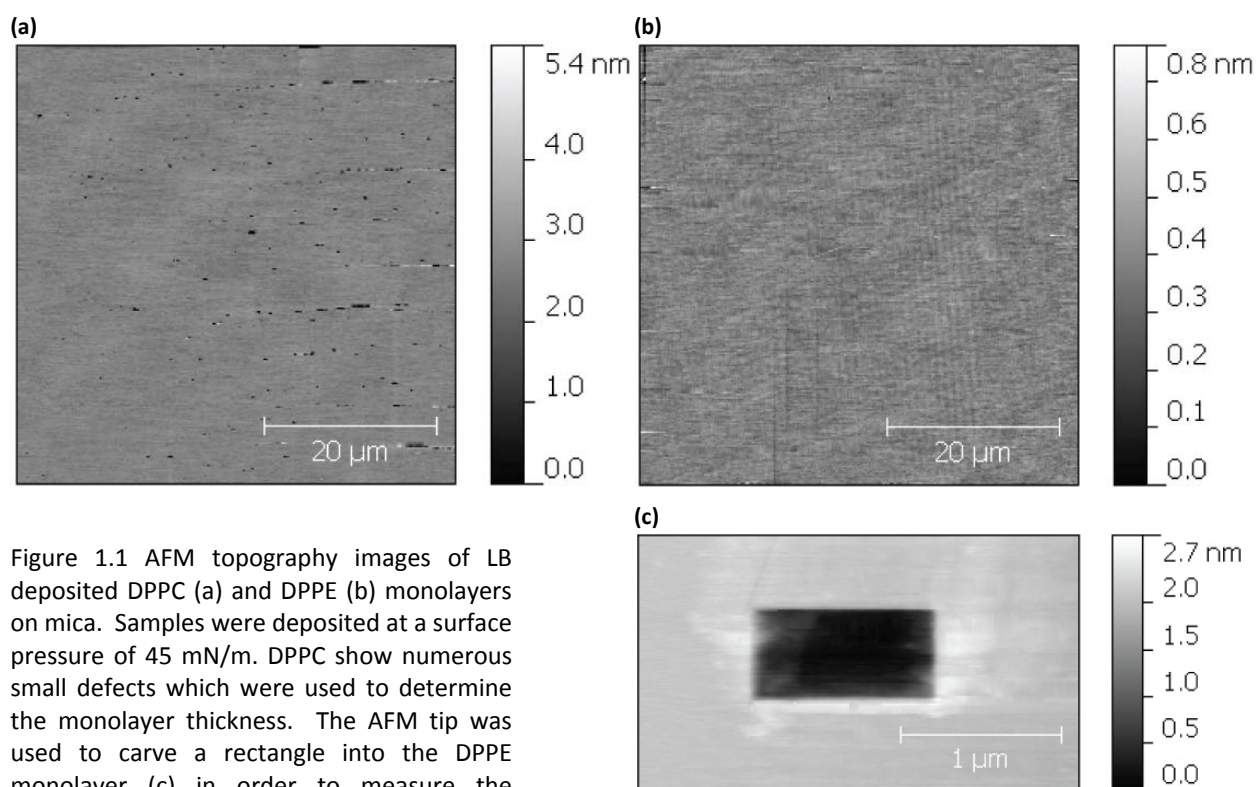
Figure 1.1 AFM topography images of LB deposited DPPC (a) and DPPE (b) monolayers on mica. Samples were deposited at a surface pressure of 45 mN/m. DPPC show numerous small defects which were used to determine the monolayer thickness. The AFM tip was used to carve a rectangle into the DPPE monolayer (c) in order to measure the thickness

To determine the DPPC monolayer thickness the difference between the minimum height of a defect and the maximum height surrounding the defect was determined for a large population of 80 defects. The depths of the defects were averaged to return the film thickness, and the uncertainty for the film thickness was taken as the standard deviation of the defect depths. For DPPE the thickness was

determined as the difference in height of the area inside and outside the carved square. The uncertainty in this thickness was determined by measuring the depth for each scan line (pixel row) that included the depression, and taking the standard deviation of these values.

X-ray Reflectivity

Specular reflectivity profiles from DPPC and DPPE monolayers on quartz are shown in Figure 1.2. The data was analyzed by dividing the monolayer film into homogeneous slabs or boxes of constant electron density and the reflectivity was calculated using the Parratt formalism [43]. Parameters corresponding to these boxes, which physically represent different portions of the lipid monolayers (headgroups and hydrocarbon tails), were then refined using the least-squared minimization method. The interfaces between slabs were smeared with variable roughness to model interfacial roughness. Specifically, the monolayer was divided into two or three boxes of different thickness and scattering length density (SLD) to represent the PE or PC headgroups (of the DPPE and DPPC lipids, respectively); tail acyl chains; and, in the case of a three box model, a water layer at the quartz interface. The parameter values describing the SLD profiles were subject to optimization against the x-ray reflectivity data by employing a weighted least-squares criterion, taking into account the uncertainties of the experimental data. The SLD of the quartz substrate was held at 22.47×10^{-6} Å^{-2} and roughness of the quartz varied from 3.3 to 3.7 Å for the various substrates and two models. The model parameter optimization was carried out by employing the software packages MOTOFIT, which runs in the IGOR Pro environment (WaveMetrics, Inc., OR) [44]. The reflectivity modeling (Figure 1.2) provided the thickness of each layer (box), SLD, and adjacent interfacial roughness (σ), enabling the structural components of the monolayer perpendicular to the interface to be resolved and compared to findings by AFM, MBI, and other scattering approaches.
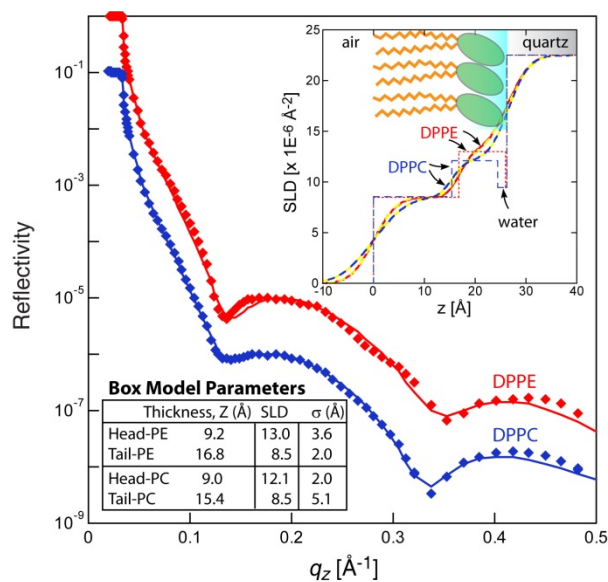
Figure 1.2 Measured x-ray reflectivity profiles of a DPPE and DPPC monolayer supported on a quartz substrate. Error bars are below the size of the data points. The solid lines are fits to the data based on the SLD profiles shown in the inset. The box model parameters are also provided. The smeared SLD profile (heavy line) reflects the roughness between the slab boxes used to represent the lipid headgroups and acyl tail region in the two box model (light dashed lines). The fit to the reflectivity data using a three box model, which included a water layer between the headgroups and quartz substrate, was indistinguishable from the two box model as shown by the overlap of the red and blue solid lines and yellow dashed lines in the SLD profile (inset). The water layer thickness was 1.8 Å with DPPC and a mere 0.3 Å with the DPPE monolayer, consistent with the greater hydration PC lipids compared to PE lipids [45, 46].

Box Model Parameters

	Thickness, Z (Å)	SLD	σ (Å)
Head-PE	9.2	13.0	3.6
Tail-PE	16.8	8.5	2.0
Head-PC	9.0	12.1	2.0
Tail-PC	15.4	8.5	5.1

Multiple Beam Interferometry

A representative spectral image of both mica contact (purple) and the monolayer contact (blue) are shown in Figure 1.3a. Figure 1.3b shows the corresponding plot of the relative intensity with wavelength averaged over the entire contact region indicated in Figure 1.3a with the dotted white line. The fringes appear as doublets due to the birefringence of mica where the peaks are split into a lower wavelength β-peak and a higher wavelength γ-peak. During experiments, we attempted to maximize the separation of the birefringent peaks to produce sharper peaks with less overlap and thus a more precise determination of the peak wavelengths.
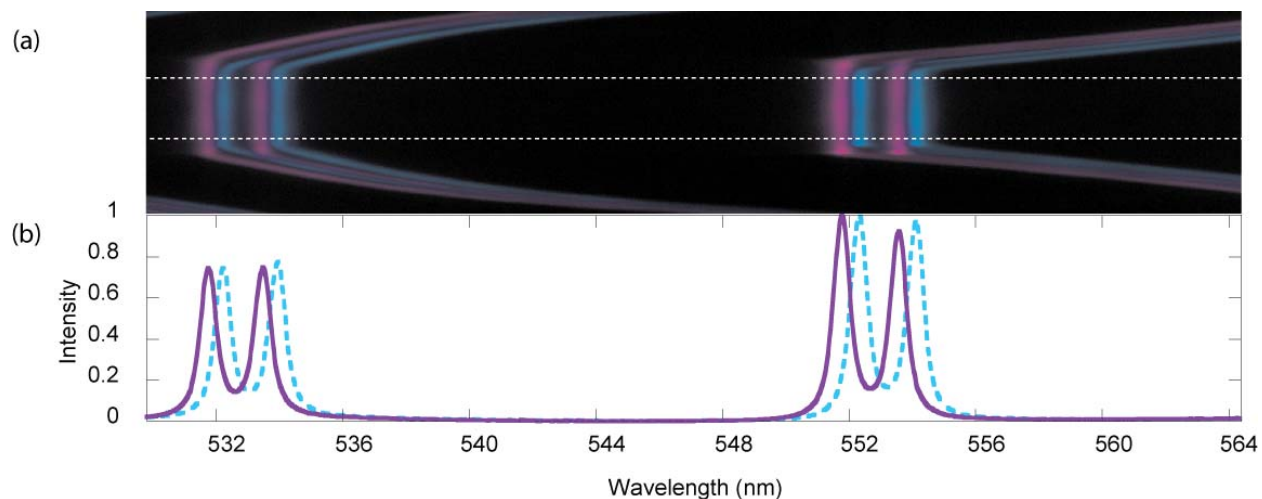
Figure 1.3 (a) Super imposed spectral images of mica-mica contact (purple) and DPPC-DPPC contact (blue). The region between the dotted lines was vertically averaged to return a spectrum for each contact. The intensity for these spectra are plotted against wavelength in (b) with mica-mica contact represented by the solid purple line and DPPC-DPPC contact represented by the dashed blue line.

The wavelengths of the measured FECO were fit using multiple Voigt peaks (convolution of Gaussian and Lorentzian), and the estimated uncertainties in the fitted peak wavelengths were less than 0.03 Å. This was determined using a Monte-Carlo error analysis where the fit was repeatedly subject to random Gaussian noise of the magnitude found in the spectra and refit to return a distribution of fitting parameters which represents the resolution of each fringe. The corresponding uncertainty in thickness and refractive index depends on the thickness of the interferometer. It can be calculated from the fringe error by simulating a population of spectra based on estimated interferometer properties with added Gaussian error of 0.03 Å standard deviation (from the error on the fringe location) and then analyzing the monolayer properties for each. Using this method we have found the resulting uncertainty in monolayer properties to be universally smaller than the variation in our measured results.

The measured fringe wavelengths are then fit to theoretical fringe wavelengths which are simulated using the multilayer-matrix method [47]. This method is derived from Maxwell's equations, and models each layer as a slab with constant properties. The optical behavior of each layer is defined with a characteristic transfer matrix which can be used to determine the transmittance as a function of

wavelength. To simplify the simulations, the beta and gamma peak wavelengths for each fringe in the experimental spectra are averaged, which allows us to treat mica with one refractive index. The fit is determined by allowing the refractive index and/or the thickness of one or more layers to vary, and then minimizing the sum-squared error between the experimental and simulated fringe wavelengths. A unique solution for the thickness and refractive index can be acquired using this method.

The thickness of the silver layer was measured during deposition and assumed to have a complex refractive index of $n = 0.0514 + (-1.0078 + .00083\lambda)i$, as has been determined for similar films [48]. Here, λ is the wavelength in Å. The spectra taken of the mica substrates in contact after removing the monolayers were used to determine the thickness, refractive index, and dispersion of the mica substrate. The wavelength dependent refractive index of mica was modeled using a two-term Cauchy equation in Eq 1.1.

$$n(\lambda) = A + \frac{B}{\lambda^2} \qquad (1.1)$$

Here, n is the refractive index, λ is the wavelength, and A and B are empirical constants. The refractive index of mica naturally varies from sample to sample, and unfortunately the thickness and both terms of the Cauchy refractive index cannot be accurately or uniquely determined simultaneously using only MBI on a mica-mica contact. The thickness and the wavelength dependent term of the refractive index can be varied simultaneously to return physically realistic values if the first term of the refractive index is known. To find the first term and an estimate of the second term, we used an Abbe refractometer to measure the beta and gamma refractive indices at two different wavelengths that span the spectrum used for MBI measurements. Six samples from different areas of our mica stock were measured and the results were used to determine both terms of the Cauchy refractive index and their respective variations.

We determined that our mica has a beta-gamma average refractive index of $n_{mica} = (1.582 \pm 0.0005) + (4.59 \pm 0.30) \times 10^5 / \lambda^2$ where λ is wavelength in Å. To analyze the mica-mica contact, we fixed the first term of the refractive index at 1.5827 and allowed the second term and the thickness to vary, which will account for any variations between mica samples and correct other systematic error that would otherwise carry over to the monolayer analysis. The uncertainty in the first term of the mica refractive index results in a maximum uncertainty in the monolayer thickness and refractive index of ±0.02 Å and ±0.0004 respectively, which are both considerably less than the variation in our monolayer properties. We are confident in the accuracy of the values obtained for the mica properties using MBI because the dispersive term of the refractive index found was within a standard deviation of the average value found for our mica stock for nearly every MBI measurement.

By removing the monolayers in situ, we ensure that the surfaces are in the same orientation and contacting at the same position for the measurements done on both the mica and the monolayer, allowing the mica properties to be fixed for the analysis of the monolayer properties. While the mica substrates have uniform properties and should ideally be independent of contact position, we have found that very slight changes in the incident angle of illumination will lead to changes in the apparent mica thickness that can be large relative to the monolayer thicknesses being determined. For this reason, we were extremely careful to ensure that neither the optics nor the orientation of the samples changed throughout the experiments. The monolayer-monolayer contact spectra were analyzed by fixing the properties of the mica and varying the monolayer thickness and refractive index. The error in the values for thickness and refractive index of the monolayer were taken as the standard deviation of all seven measurements for each monolayer.

Discussion

The results of the MBI, AFM and XRR experiments done in this work are shown in Table 1.1. The refractive indices measured using MBI were used to estimate the Hamaker constant (A_H) for each lipid in water for comparison with measured values of the Hamaker constant between lipid bilayers, using the equation [49]

$$A_H \approx \frac{3}{4} k_B T \cdot \left(\frac{\varepsilon_1 - \varepsilon_3}{\varepsilon_1 + \varepsilon_3}\right)^2 + \frac{3 h \nu_e}{8\sqrt{2}} \cdot \frac{(n_1^2 - n_3^2)^2}{2 \cdot (n_1^2 + n_3^2)^{3/2}} \qquad (1.2)$$

Here, ε is the permittivity, n is the refractive index, ν_e is the ionization frequency (assumed to be 3×10^{15} Hz), and the subscripts 1 and 3 refer to the lipid and water, respectively. We assumed the permittivity of the lipid to be the refractive index squared. The uncertainty of the Hamaker constants was calculated using the uncertainty of the refractive index for the corresponding lipid.

Table 1.1 Measured lipid monolayer properties

| | Thickness (Å) | | | | |
Lipid	MBI	AFM	XRR	Refractive Index	Hamaker Constant (J)
DPPC	23.9 ± 0.5	24 ± 6	24.4	1.478 ± .006	$(6.9 \pm 0.5) \times 10^{-21}$
DPPE	25.5 ± 0.6	25 ± 1	26.0	1.485 ± .007	$(7.5 \pm 0.6) \times 10^{-21}$

The DPPE and DPPC thicknesses determined using these three different methods are all in excellent agreement. Both the AFM and XRR thickness values are within error of the MBI measurements demonstrating that MBI is a viable alternative to these techniques with the added capability of simultaneously measuring the refractive index.

Table 1.2 shows a collection of DPPE and DPPC monolayer thickness measurements from the literature for comparison with our results. Measurements of thickness taken from bilayers or monolayers at a hydrophobic solid-water interface [6, 12, 21, 50] are not included because they are not representative of the system being studied by us; however, the measurement of lipid monolayers on a hydrophobic surface consistently showed thicker monolayers which is likely due to the hydration or protrusion of the

outer leaflet being incorporated into the thickness [6, 7]. X-ray scattering techniques are not susceptible

to this effect and are also included for comparison to our own thickness measurement regardless of

interface or geometry.

Table 1.2 Thickness measurements from literature

Lipid	Measurement Technique	Interface	Pressure (mN/m)	Thickness (Å)	Source
DPPC	MBI	Mica/Air	45	23.9 ± 0.5	This work
	Lamellar XRD	Hydrated Multilamellar Vesicles (MLV)	--	21	[17]
	x-ray shadowing	Monolayer at Silica/air	30	25 ± 3	[2]
	XRR	Monolayer at Air/water	>40	24.6	[16]
	XRR	Monolayer at Air/water	35	24.2	[19]
	Various scattering techniques	MLV and Unilamellar Vesicles (ULV)	--	23.9	[18]
	AFM	Mica/Air	2*	24	[5]
	AFM	Mica/Air	40	29 ± 2	[21]
	Calculated from area per molecule	Bilayer/Water	--	23 ± 1	[6]
DPPE	MBI	Mica/Air	45	25.5 ± 0.6	This work
	Lamellar XRD	Hydrated MLV	--	24.5	[17]
	XRR	Air/Water	40	25.5	[19]
	AFM	Mica/Air	40	28 ± 2	[21]
	Calculated from area per molecule	Bilayer/Water	--	27 ± 1	[6]

*This pressure is in the phase coexistence region for DPPC. Measurements of thickness were taken for a solid phase domain.

The thickness measurements of the DPPE and DPPC monolayers returned expected results with

DPPE being thicker than DPPC, which reflects the tilted structure of DPPC [17, 51, 52].   They are also

within the range of values found from various techniques in the literature. In particular, our results are

very similar to those measured using x-ray scattering on monolayers at similarly high surface pressures.

The low error in our thickness measurements show that the results are repeatable and of the resolution

typically expected from SFA thickness measurements. The errors for both refractive index and thickness

represent the physical variation in the monolayer properties as opposed to the error caused by the SFA resolution limit because this was the dominant source of error. The lowest resolution sample we measured had uncertainty estimates of ±0.263Å and ±0.0057 in thickness and refractive index respectively.

The values obtained for the monolayer refractive indices are as expected relative to one another, with DPPE having a higher refractive index due to higher molecular packing. There are very few measurements of the refractive index of oriented lipids to compare with, and to the best of our knowledge no reported measurement of the refractive index of pure DPPE or DPPC monolayers. The value often used as the refractive index for these lipids is that found by Cherry and Chapman [13] for a black lipid membrane of egg lecithin in which these authors report a value of 1.464 ± 0.004 for the normal refractive index and a thickness of 62 ± 2 Å. The refractive index values found here using MBI are higher than this for both DPPE and DPPC lipids. Theoretical predictions also show a higher normal refractive index for solid phase tilted DPPC [53] and for ordered, saturated fatty acid chains [15]. The inconsistency between these experimental results is not surprising because the lipids are not identical, nor are they arranged or prepared identically. The black lipid membranes were prepared with an n-decane solvent which can remain dissolved within the membrane after spreading and has a lower refractive index of 1.412. If we assume the thickness found here for DPPC is equal to the thickness of an egg PC monolayer and that results from Cherry and Chapman represent an average of the refractive indices weighted by the thickness of the bilayer and dissolved n-decane, we can back-calculate the refractive index of the isolated lipids using

$$n_{lipid} = \frac{t_{mix}n_{mix} - t_{decane}n_{decane}}{t_{lipid}} \qquad (1.2)$$

Here the subscript "mix" denotes the combination of lipids and n-decane. This returns a lipid refractive index of 1.479 which is well within error of the refractive index determined here for DPPC. This explanation is contradicted by more recent findings that the n-alkane solvent molecules can be

incorporated into the lipid membrane and can actually induce higher packing and less tilt [4, 10, 14, 45, 46, 54, 55]. Such behavior could explain the higher thickness found by Cherry and Chapman, but not the lower refractive index, as this should increase with molecular packing. Another likely source of discrepancy is the inclusion of water in their reflectivity measurements due to protrusion, hydration and undulations in the membrane, which would explain both a larger thickness and lower refractive index as was found for the black lipid membranes.

The value for the Hamaker constant measured between DPPC bilayers in water by Marra and Israelachvili [6] of $(7 \pm 1) \times 10^{-21}$ J further supports a higher refractive index value. This result is very close to our estimated Hamaker constant for DPPC in water, while the estimated Hamaker constant for the refractive index of 1.464 from Cherry and Chapman [13] yields a lower Hamaker constant of $(5.7 \pm 0.3) \times 10^{-21}$ J. This suggests that the use of the latter refractive index is inappropriate for solid supported lipid bilayers.

The hydration of SLBs is an area that has received considerable attention. In particular, the 'water-gap' between the inner-leaflet and substrate has been reported to have thicknesses ranging from a few to over 10 water layers [45, 46, 56-59]. The thicknesses we have found for DPPE and DPPC suggest that the water gap is on the lower side of previous measurements. Our system differs from others in that the lipid monolayers are in dry air after deposition whereas the water gap has only been measured on SLBs and multilayers in bulk water. However, our findings show that there is no observable change in the hydration of the monolayer after introducing bulk water to dry monolayers in contact, even though this procedure was expected to hydrate the head groups through defects in the monolayer. It is possible that the water cannot penetrate between the head group and substrate while the surfaces are in a hard contact, and separating the wet surfaces will result in rearrangement or damage and an unusable sample. It is also possible that the monolayers are already saturated, and the layer is simply obscured by the hydration layer that natively exists at the mica surface which is unavoidably incorporated into to mica

thickness used to calculate the monolayer properties. Two mica surfaces in contact have been found to have an equilibrium hydration gap of 2.2 Å in pure water and up to 11 Å in sufficiently concentrated inorganic salt solutions [60] (although recent findings suggest this hydration layer could be thicker [61]). This will mask up to 5 Å of water between the monolayers and mica. The hydration of the monolayer head group cannot be distinguished from the overall monolayer using MBI and cannot be estimated without a known refractive index of the monolayer free of hydration. However, at the very least, it can be deduced from (1) the similarity of our results to the x-ray scattering thickness measurements on vesicles and at the air-water interface (which are not obscured by hydration or substrate roughness) and (2) the high refractive index of our monolayer, that dry DPPE and DPPC monolayers have a considerably smaller 'water gap' than measurements on multilayer systems suggest. We have also found that the monolayer thickness is the same for monolayers that were originally part of a bilayer which was stripped of its outer leaflet by draining water from the system. We expected these monolayers to be fully hydrated because no steps were taken to dry them. That they exhibit the same properties as the dried monolayers supports the idea that the dried monolayers were still hydrated after drying, and that the hydration cannot be removed by drying with P_2O_5. Whether the hydration was reduced upon draining is not clear because we have no measure of the hydration gap for the original bilayers.

Conclusions

The thickness and refractive index of mica supported monolayers of DPPC and DPPE were simultaneously determined using MBI. The values found for the thickness were 23.9 ± 0.5 Å and 25.5 ± 0.6 Å, respectively, which are consistent with results found using various x-ray scattering techniques for lipids at high surface pressure. The refractive index values for DPPC and DPPE were 1.478 ± 0.006 and 1.485 ± 0.007, respectively, results which are greater than the value measured on black lipid membranes of egg lecithin by Cherry and Chapman [13] of 1.464 ± 0.004. Our results are supported by the similarity between experimental Hamaker constant found for DPPC bilayers in water [6] and the Hamaker constant

estimated from the DPPC monolayer refractive index measured here. Additionally, our results indicate that the water gap that has been observed between the lipid head groups and the substrate in lipid bilayer systems may be different for different lipid and substrate systems. While absolute measurements of the water gap between the hydrophilic substrate and the head group is not possible using MBI, the thickness and refractive index result found here suggest that the water gap is thinner for PE and PC monolayers than has been found for SLBs. These results illustrate the potential necessity of distinguishing the properties of different lipid systems and how they are supported.

Acknowledgments

Chapter II

Analyzing refractive index profiles of confined fluids by interferometry

Daniel F. Kienle and Tonya L. Kuhl*
Department of Chemical Engineering and Materials Science, University of California Davis, 95616, USA
*Corresponding author. E-mail: tlkuhl@ucdavis.edu

Abstract

This work describes an interferometry data analysis method for determining the optical thickness of thin films or any variation in the refractive index of a fluid or film near a surface. In particular, the method described is applied to the analysis of interferometry data taken with a surface force apparatus (SFA). The technique does not require contacting or confining the fluid or film. By analyzing data taken at many inter-surface separation distances out to at least 300 nm, the properties of a film can be quantitatively determined. The film can consist of material deposited on the surface like a polymer brush, or variation in a fluid's refractive index near a surface resulting from, for example, a concentration gradient, depletion in density, or surface roughness. The method is demonstrated using aqueous polyethyleneimine (PEI) adsorbed onto mica substrates, which has a large concentration and therefore refractive index gradient near the mica surface. The PEI layer thickness determined using the proposed method is consistent with the thickness measured using conventional SFA methods. Additionally, a thorough investigation of the effects of random and systematic error in the SFA data analysis and modeling using simulations of SFA data is described in detail.

Introduction

The structural properties of fluids confined between solid surfaces are valuable for interpreting fluid behavior as continuum theory breaks down. When coupled with force measurements, the changes in the fluid refractive index can shed light on the mechanism of elusive surface interactions such as hydration, hydrophobic, or solvation interactions. For example, such measurements could be used to determine the properties of a depletion layer near a surface like that found for water near a hydrophobic surface [62-65]. Likewise, the same approach can be applied to any adsorbed or deposited film to determine the film's thickness or refractive index and quantify the properties of any polymer, surfactant or thin-film of interest. The SFA is an ideal instrument for this purpose because it is capable of simultaneously measuring the interaction between macroscopic surfaces and density (via refractive index) of the medium separating these surfaces. However, such measurements are challenging due in particular to systematic error which arises from uncertainty in substrate properties and the effects of inhomogeneity in the fluid or film refractive index that is not typically accounted for in optical analysis.

Several complementary techniques are useful for measuring properties of the thin films and fluids near surfaces. Ellipsometry [66], is able to give adsorbed mass, but is difficult to apply to measurements in solution. Quartz crystal microbalance is capable of giving real time estimates of the adsorbed amount, and X-ray and neutron scattering techniques [67] are capable of measuring local refractive index profiles near surfaces. However, measurement in confinement is not straight-forward, and has only been rarely accomplished with X-ray and neutron reflectivity [68-73]. While the SFA cannot measure the local refractive index normal to the surface, the mean refractive index can be measured throughout confinement, which can elucidate the effects of confinement.

The SFA has been applied to refractive index profile measurements (measurements taken at many separation distance) of confined polymer solutions [74], water [38, 75, 76], and hydrocarbons [77, 78]. Kekicheff and Spalla [38] demonstrated how uncertainty in the substrate contact measurements can

21

cause systematic error in the refractive index that is indistinguishable from true variation of the refractive index. These results call into question the accuracy of other refractive index profile measurement. The extended SFA takes advantage of advances in technology to more precisely determine the mica substrate properties, and the reduction of random error using this SFA setup has been demonstrated [79]. However, errors in substrate properties can have many other potential sources including particle contamination [77, 80, 81] and adsorbed contaminants [77, 82-87], which will have the same effect on the refractive index measurements as that described by Kekicheff and Spalla [38]. In a later paper Heurberger et al. [77] demonstrated how contradictory refractive index profile results can be acquired for surfaces with and without particle contamination.

This work describes an algorithm for determining solvent, adsorbed layer and/or substrate properties without contact measurements. This is useful for several systems of interests where the surfaces are fragile and could be damaged or changed by contacting them. For example, hydrophobic monolayers in water can be torn apart upon separation and unstable bilayers are susceptible to fusion [88, 89]. It is also useful for systems where changes such as plastic deformation or permanent chemical reaction may take place upon contact. Furthermore, the method could potentially be used to ascertain the roughness or lateral heterogeneity of surfaces or films. The technique works by eliminating the effects of systematic error caused by inconsistencies between contacted measurements and refractive index profile measurements. We demonstrate the technique theoretically using realistic simulations with added random and systematic error typical of SFA experiment, and physically with experiments on an aqueous solution of cationic polyethyleneimine adsorbed onto mica substrates as a model of a medium with variations in the refractive index.

Experimental

Linear PEI hydrochloride salt with a molecular weight of 20,000 and a PDI of 1.2 was purchased from Sigma-Aldrich and stored at 4 °C. The polymer was dissolved in water to form a 100 ppm solution by weight. The water used throughout these experiments was purified with a MilliQ gradient water purification system with a resistivity of 18 MΩ·cm.

The SFA substrates consisted of back-silvered, thin mica sheets of uniform thickness. The mica was cleaved and cut using the procedure described by Israelachvili et al. [84]. The mica substrates were glued silver-side-down onto two cylindrical glass discs and mounted in the SFA opposite one another in a crossed cylinder orientation, where they form an interferometer. A droplet of the PEI solution was applied between the surfaces and left for several hours. Then, the SFA box (350 ml) was filled with 0.5 mM $NaNO_3$ solution and left over night. Under these conditions the surface coverage should be laterally homogeneous [90]. White light from a tungsten halogen source was collimated and shone through the interferometer which transmits whole order wavelengths called fringes of equal chromatic order (FECO) [91]. The light is then directed into a spectrometer so the peak wavelengths can be measured and used to analyze the properties of the system.

All data analyses were done using software written in-house that determines layer properties numerically. The measured fringe wavelengths were fit to theoretical (simulated) fringe wavelengths by varying up to two properties of the system (in our case the thickness and refractive index of the central film), to minimize the sum-squared error between the measured peak wavelengths and theoretical peak wavelengths. The theoretical spectra were generated using the multilayer matrix method [33, 47] which uses optical transfer matrices to describe the propagation of electromagnetic waves in each layer of a stratified medium. This method is derived from the Maxwell equations and is very flexible with regard to the properties of the system. Mica is birefringent which causes each FECO to appear as a doublet with a β-peak and γ-peak. To reduce the number of computations, we use the midpoint of the fitted β and γ

peak wavelengths as the measured peak wavelength. The experimental set-up and data analysis for SFA measurement has been described in greater detail previously [92].

Spectra were measured in flattened contact before and after adding the polymer solution to determine the substrate and compressed polymer properties. For each profile, measurements were taken from beyond 4000 Å separation to flattened contact. The measurement taken for this experiment had up to nine beta-gamma fringe doublets. Only fringes that remained in the spectrum at all separations distances were used in the analysis (typically 6-7 fringe pairs). The spectral data for non-contact measurements represents the lateral average of several square-microns surrounding the point of closest approach between the curved surfaces and are taken using exposure times of several seconds. An example spectrum from separated surfaces is shown in Figure 2.1b. Measurements on surfaces in flattened contact (Figure 2.1a) are averaged over a larger area to increase the signal to noise ratio. We were careful to ensure that neither the optics nor the orientation of the surfaces were altered between the contact and non-contact measurements, because even slight changes in either can cause significant changes in the apparent properties of the substrate [92].
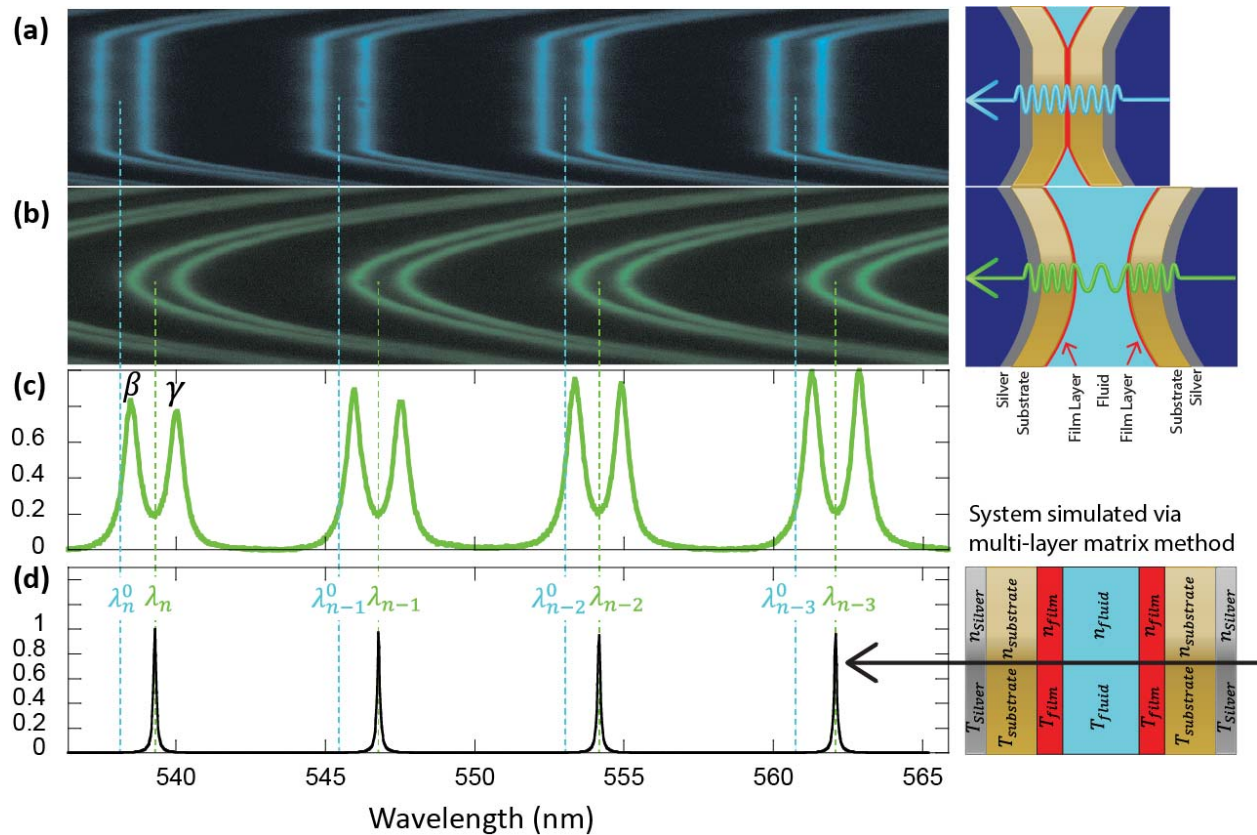
Figure 2.1 Examples of a spectral images with surfaces in compressed contact (a) and with surfaces separated (b). The spectrum of the separated image used for analysis is shown in (c) and the best fit theoretical spectrum is shown in (d), where the green dashed lines indicate the midpoint of the experimental β and γ peak wavelength used to define the experimental fringe position to which the theoretical fringes were fit. To the right of (a) and (b) are illustrations of the interferometer and to the right of (c) is a schematic of the system used to simulate the theoretical spectrum.

Before describing the algorithm in detail, we first address sources of random and systematic error and their corrections in order to obtain quantitative measurements of the surface film or confined material properties from interferometer spectra.

Random Error in SFA

The random error in the fringe wavelength can be determined from the measured spectra (Figure 2.1) [92]. Using a Monte-Carlo type error analysis, we have determined what the effect of random error in the fringe wavelengths (Gaussian noise of 0.03 Å standard deviation) has on the refractive index and thickness when analyzed simultaneously at different separation distances, each with 500 iterations. The results shown in Figure 2.2 reveal a periodic pattern in error sensitivity of both the thickness and refractive

index with enhanced sensitivity at separation distances of zero and around even multiples of 1000 Å, and

reduced sensitivity around odd multiples of 1000 Å. This 2000 Å period in wavelength corresponds to the

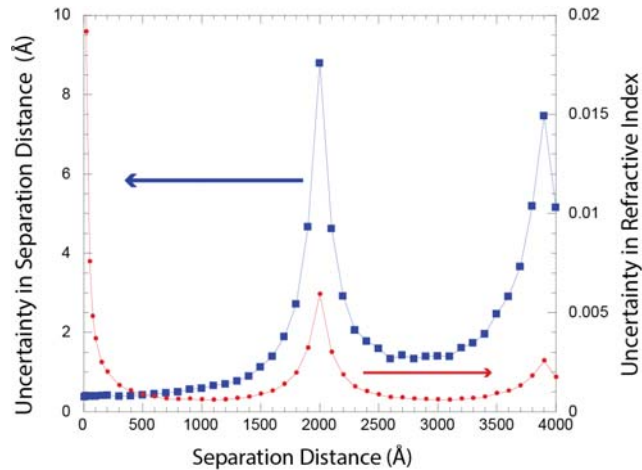average inter-fringe distance of the contact spectrum.

Figure 2.2 Theoretical uncertainty of separation distance (blue squares) and refractive index (red circles) as a function of true separation distance. Uncertainty was result of random error on the substrate contact and profile fringe measurements, determined by simulating and analyzing fringe data with added Gaussian error, iteratively, and taking the standard deviation of the results.

Systematic error

One of the most important and identifiable systematic errors in the SFA is inaccuracy in the

substrate properties. The other is inconsistency or changes in the properties of the central film between

the substrates that is unaccounted for. This can be caused by adsorption or removal of materials localized

at the substrate between contacted and separated measurements or by variation in the fluid refractive

index that exists at the substrate surface when separated but is displaced or changed when in contact.

These systematic errors can be broken into three categories that exhibit different functionality. The first

type results from using incorrect values for the substrate properties which are still an acceptable solution

to an accurate substrate contact spectrum. This type of error arises from simultaneously varying thickness

and refractive index of the substrate when analyzing the substrate contact spectrum, or fixing the

refractive index of the substrate at an incorrect value, and it results in a constant offset in the refractive

index of the intervening material and a proportional offset in the separation distance such that $\Omega_{error} \approx$

Ω_{actual} where Ω is the optical thickness (Ω = T × n, where T is the layer thickness and n is the layer

refractive index) of the fluid. This will be referred to as type 1 error and is shown in Figure 2.3a (thick blue

dashed line) where an incorrect value of the refractive index of mica was used resulting in a constant shift

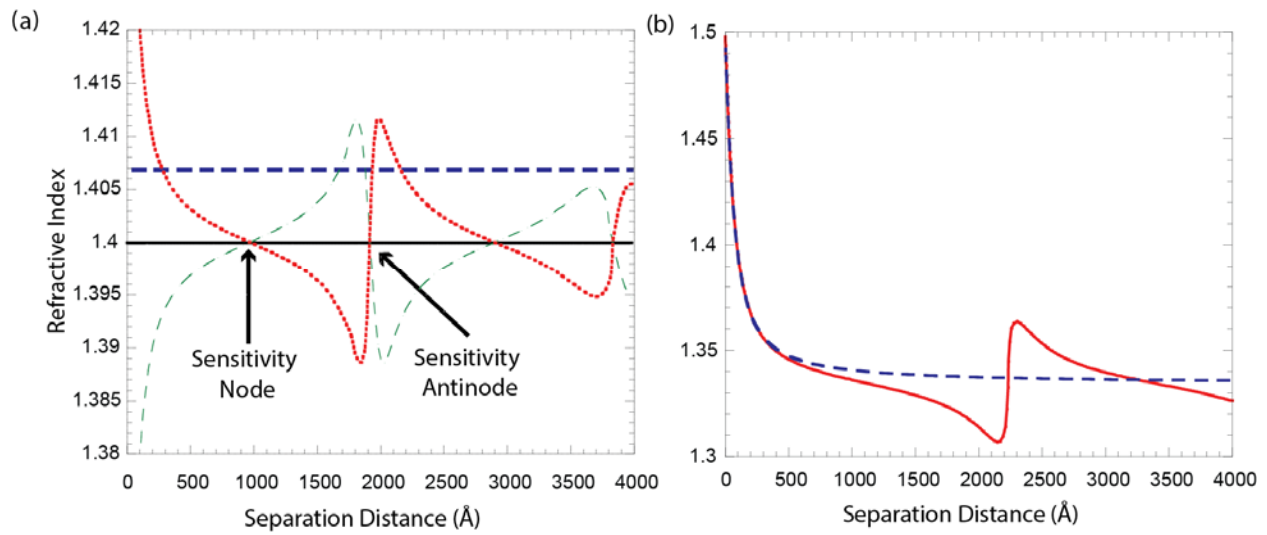of 0.007 above the true optical thickness (solid black line).

Figure 2.3 Systematic error on the fitted refractive index profile as a function of simultaneously fitted separation distances (note that the refractive index plotted is the mean value for the material between the substrates). Error caused by (a) incorrect substrate thickness or refractive index with the correct optical thickness (type 1 error; thick blue dashed line); or a type 2 error in optical thickness above (thin green dashed line) and below (red dotted line) the true optical thickness (solid black line). Data was generated by simulating fringes and analyzing them with mica properties fixed at incorrect values. (b) Type 3 systematic error resulting from analyzing variable refractive index fluid with the mean refractive index at each separation distance (solid red line) along with the actual mean refractive index of the fluid (blue dashed line). Data was generated using simulation method described in simulation methods and results section.

The second type of error (type 2 error) results from using inaccurate or inappropriate contact

fringe wavelengths as a result of contamination, or unaccounted-for shifts in the optical path due to

alterations in the optics or orientation of the substrates to determine the properties of the substrate. It

results in a periodic trend in the refractive index with a period of around 2000 Å, similar to the random

error (Figure 2.2), with an erroneous variation in the mean refractive index at low separation distances. This is shown in Figure 2.3a, where the red dotted line is the result of underestimating the substrate thickness and the thin green dashed line is a result of overestimating the substrate thickness. As expected the refractive index converges to the true value at the separation distances of low error-sensitivity (henceforth referred to as sensitivity nodes) and diverge at the separation distances of high error-sensitivity (henceforth referred to as sensitivity antinodes). This is problematic for refractive index measurement because data at distances below the sensitivity nodes will appear to be converging toward a bulk value and variations in the refractive index are difficult to distinguish from type 2 systematic error. Unfortunately no previous refractive index profile measurements extend beyond the sensitivity node [38, 74, 77, 78], so the resulting divergence has not been observed. If type 2 error is present in the analysis, type 1 error will also be present unless the substrate refractive index is accurate, in which case the sensitivity nodes will reflect the bulk refractive index of the fluid.

Type 2 error has been addressed in part by Kekicheff and Spalla [38] for water confined between hydrophobic surfaces and was attributed to the uncertainty in the substrate measurement. While the technological and analytical advances have reduced this uncertainty from their error of ±1 Å wavelength (which was even large at the time) to less than ±0.03 Å depending on the system specifics, we believe that the inaccuracies leading to this type of error are not purely a result of random uncertainty in substrate measurement being propagated in the analysis of subsequent layers as suggested, but are in fact primarily systematic. This type of error may be caused by contamination such as particles [80, 81] or adsorbed molecules [83-85, 87, 93, 94] on the surface during contact, or by any other inconsistencies between the substrate contact measurement and separated profile measurements such as changes in the optics. Furthermore, it is known that there is a layer of ions on mica surfaces after cleaving that can be removed by rinsing [76]. It is also known that mica surfaces in water are hydrated even when in adhesive contact [60]. It also requires considerable pressure to displace solvent [95, 96] or electrolytes [97] from between

confining surfaces which could compress and alter the apparent properties of the substrate if achieved. Thus, in many common experimental scenarios, there is a strong possibility that measurement of substrate properties will include adsorbed layers, even when the surfaces are free of contamination. This is generally unimportant for distance and force measurements due to the small thickness of such adsorbed layers in most systems but will have a dramatic impact on the refractive index measurements throughout the entire profile.

Type 3 error results from treating fluids with a continuously varying refractive index as a homogeneous film of identical thickness with the refractive index equal to the mean value within the film, or ignoring adsorbed films (polymers, surfactants etc.) on the substrate during analysis. This approximation is convenient for use of matrix methods that dramatically simplify the analysis of layered optics. Although it was used in this research for refractive index measurements in the SFA, this approximtion ignores reflections from within the film due to refractive index gradients, which can significantly impact the refractive index values even if the gradients are not extreme [98]. Regardless, if the substrate measurements are accurate, simulations indicate that the mean refractive index profile is within ± 0.001 out to separation distances of 400 Å (disregarding random error) as shown in Figure 2.3b. This is typically the range of interest for SFA experiments. However, the oscillations from type 2 error are still present as a result of assuming the refractive index is constant, as can be seen at larger separations in Figure 2.3b. In other words, the variation in the mean refractive index at small separation distances is not the result of systematic error, but the periodic trend at larger separations is. The profile is indistinguishable from type 2 error at separation distances greater than where the refractive index variations at either surface overlap (henceforth referred to as the overlap separation distance). If the surfaces reach contact at zero separation distance, then it is reasonable to conclude that the refractive index variation is not a result of substrate error and that there is no type 2 error. On the other hand, if they contact at a positive separation distance, there is no way to deconvolute type 2 and type 3 error.

The analytical method described in this paper focuses on correcting type 1 and type 3 error while assuming that type 2 error is negligible, which is appropriate for clean, carefully prepared mica substrates [84].

Algorithm for Correction of Systematic Error

The analytical method presented here uses data at many separation distances throughout the profile to add the constraint that the local refractive index is constant away from the surface. In other words, measurements must be made beyond the overlap separation distance. This allows three properties (including refractive index, thickness, and dispersion of any layer) to be determined, one that is constant throughout the profile and two that vary at each separation distance. In addition to these three variables, the specific substrate properties can be determined, as long as they are still a solution to an accurate substrate contact measurement.[a] Finally, this can all be done without taking measurements below 1000 Å (except the substrate contact), which is useful for determining properties of films that may be damaged or altered when put into contact.

The method used to correct systematic error takes advantage of the fact that the perturbation of the refractive index at separation distances greater than the sensitivity node is not influenced by variations that occur upon confinement. Thus, we can find substrate and deposited layer properties where the refractive index is constant at a known bulk value. If there are inherent variations in the fluid refractive index near the substrate or there is a film on the substrate, a hypothetical 'transition layer' (tl) with appropriate properties can be added between the substrate and solvent to counteract the inherent variation. This method is appropriate because an inhomogeneous or stratified film is optically equivalent to two homogeneous films [98]. Incorporating the transition layer redefines the plane of contact from the substrate-substrate contact to layer-layer contact. To fully account for type 3 error, the properties of the transition layer must satisfy

---

[a] A substrate contact measurement alone can only be used to determine either the substrate thickness or refractive index, while the other is fixed at an assumed value or measured using another method.

$$\Delta\Omega = T_{tl}(n_{tl} - n_{bulk}) \approx \int_0^\infty (n_{local}(z) - n_{bulk})dz \qquad (2.1)$$

where $\Delta\Omega$ is the change in optical thickness, T_{tl} is the thickness of the transition layer, n_{tl} is the refractive index of the transition layer, n_{bulk} is the bulk refractive index, n_{local} is the local refractive index and z is the normal distance from the surface. These parameters are shown schematically in Figure 2.4. The change in the optical thickness is analogous to the areal change in mass from bulk.

The refractive index profile found by incorporating the transition layer does not have a direct physical meaning because the transition layer effectively cancels any refractive index variations leaving a central film with a constant, bulk refractive index in the region between the substrates. However, because the thickness of the region over which the actual refractive variation occurs may not match the thickness of the transition layer, there will be a compensatory deviation from bulk refractive index at separations below the overlap separation distance (see Appendix Figure A.2). As a result, the onset of this deviation corresponds directly to the distance from the surfaces over which the true, local variation in the refractive index extends. If the mass of the heterogeneous region is conserved during confinement as is expected for deposited or compressible films, there will be no deviation. The actual mean refractive index profile can then be calculated using

$$n_{act} = \frac{Dn_{fit} + 2T_{tl}n_{tl}}{D + 2T_{tl}} \qquad (2.2)$$

where n_{fit} is the refractive index profile fit with the transition layer and D is the separation distance between the transition layers. Figures showing

The algorithm works in two main steps. The first step is to determine the specific substrate properties. This makes use of the sensitivity nodes which should equal the known bulk refractive index of the solvent regardless of any type 2 or type 3 error. To do this the substrate refractive index is varied and the substrate contact measurement is reanalyzed to return thickness and dispersion of the substrate

at each iteration. Then the sensitivity nodes are found and the difference between the nodes and known

bulk fluid refractive index is minimized according to the fitting argument

$$arg = \Sigma(n_{node,i} - n_{bulk})^2 \qquad (2.3)$$

Here $n_{node,i}$ is the refractive index at the ith sensitivity node. Although only one sensitivity node is needed

for this step, results will be less susceptible to random error if more are used.

The sensitivity nodes can be approximately found by determining the separation distance at which

the fringes most closely bisect two contact fringes, which is accomplished by minimizing the argument

described by

$$arg = \Sigma \left| \lambda_n - \frac{\lambda_{n-1}^0 + \lambda_n^0}{2} \right| \qquad (2.4)$$

In this equation λ_n is the wavelength of the nth fringe and λ_n^0 is the wavelength of the nth contact fringe.

Alternatively, the sensitivity nodes occur where the difference between the odd-even inter-fringe

distance and the even-odd inter-fringe distance is maximized. This is useful for experiments where

contact fringes cannot be acquired, and the sensitivity nodes can be found by maximizing the fitting

argument

$$arg = \Sigma|2\lambda_n - \lambda_{n-1} - \lambda_{n+1}| \qquad (2.5)$$

An accurate estimate of the node distance can be found by fitting the argument, within a few hundred

angstroms separation distance of each node, to a quadratic equation and finding the maximum.

The second step of the analysis determines the optical thickness of the transition layer by

minimizing the standard deviation of the fluid refractive index around the sensitivity antinode. This is done

systematically by using data between the first and second sensitivity nodes. At the solution, the

divergence of the refractive index at the sensitivity-antinodes is eliminated and any type 3 error is

corrected. The specific refractive index and thickness (n_{tl} and T_{tl}, respectively) of the transition layer

cannot be found independently. Instead, the transition layer refractive index is fixed at an estimate, and the thickness is varied. Solutions are best found with a direct search algorithm when using this method. In reality, the resulting ΔΩ has a weak linear dependence on the estimate of the refractive index of the transition layer. In systems we have measured and simulated, the deviation in ΔΩ resulting from fixing the transition layer refractive index at an inaccurate value is below the uncertainty in our results for a large range of transition layer refractive indices (± 0.25). However, considering that the dependency of ΔΩ on n_{tl} will be different between differing systems, it is important to verify that the effect of this dependency is not significant, particularly for experiments where the transition layer refractive index cannot be estimated within a narrow range. This can be done simply by running the second step of the analysis with the transition layer refractive fixed at different values. Our simulations indicate that the deviation of ΔΩ is roughly equal in magnitude to the inaccuracy of the refractive index estimate, while the sign of the deviation depends on the sign of ΔΩ. The quality of the fit shows negligible dependence on the refractive index estimate, so this trend does not present a means of determining the transition layer ΔΩ and refractive index independently.

A schematic of the full algorithm and an illustration and description of the results are shown in the supporting information sections S1 and S2 respectively. After the second step in the analysis, the full profile of refractive index data is reanalyzed with the corrected substrate refractive index and added transition layer, and the full mean refractive index profile can be calculated using Eq 2.2.

Simulation Methods and Results

The correction method was first tested using realistic, simulated data based on an aqueous system with an adsorbed layer of PEI on the mica substrates. The error-free refractive index profile fringes and substrate contact fringes were generated using the multilayer-matrix method from specified interferometer properties. Data was generated for a system with variable refractive index describe by Eq 2.6 where z is the distance from the substrate:

$$n_{local} = (1.5 - 1.334)e^{-z/20} + 1.334 \qquad (2.6)$$

This exponentially decaying refractive index profile was chosen as a simple model for the adsorbed PEI layer in water, where the bulk refractive index of PEI is set to 1.5.

The inclusion of a variable refractive index film away from the substrate can be modeled using a power series to approximate the non-analytical expression for the electric field that arises from including normal variations in the refractive index. With this approximation, and using a second order expansion, the characteristic matrix of a non-homogeneous dielectric film with normal incidence can be written as

$$\boldsymbol{M}_{heterogeneous} = \begin{bmatrix} 1 - k^2 \int_0^d n^2 \mathcal{B} \, dz & -ik\mathcal{B} \\ -ik\mathcal{A} & 1 - k^2 \int_0^d n^2 \mathcal{A} \, dz \end{bmatrix} \qquad (2.7)$$

Here, k is the wavenumber, n is the refractive index, z is the distance normal to the surface, d is the thickness of the layer, and M is the transfer matrix for use in the multilayer matrix method [47]. The Functions A and B are defined as

$$\mathcal{A} = \frac{1}{Z_0} \int_0^z n^2 dz \qquad (2.8)$$

$$\mathcal{B} = Z_0 z \qquad (2.9)$$

where Z_0 is the impedance of free space. A detailed derivation of these equations and higher order expansions are described by Jacobsson (section 3.1) [98].

This method is accurate for thin films with low order expansions [98] in k. In the case of a fluid between two surfaces with inherent refractive index variation near the surfaces, the fluid layer can be broken into 3 layers: a homogeneous film at the bulk refractive index, sandwiched between two heterogeneous films, as shown in Figure 2.4. This keeps the length scale of the heterogeneous films small, allowing for accurate solutions with a low order expansion, even at large separation distances. It is important to note that the heterogeneous films at either surface cannot be treated as identical and thus the system has to be analyzed as an asymmetric interferometer. For systems where the heterogeneous

film extends far into the fluid, higher order expansions are required. Further expansion is tedious but straightforward [98]. A simple way to check whether a higher order expansion is necessary is to simulate fringes using the equations above, and compare them to a system where the fluid is modeled by a large number of thin homogeneous layers. This is a simple, but computationally expensive extension of the multilayer matrix method. A model including terms up to powers of k^4 was necessary for the simulations in this study, because the heterogeneous slabs extended far into the central fluid and substantial inaccuracies were observed when lower order expansions were used.
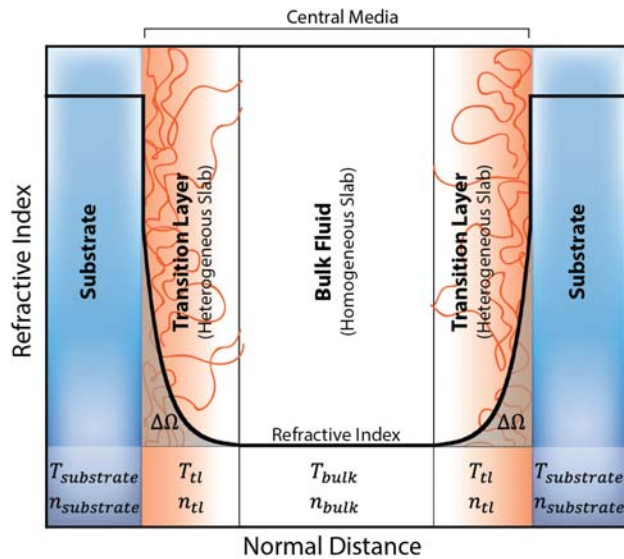

Figure 2.4 Plot of the local fluid refractive index with normal position through a model sample. Each slab would be represented by a different characteristic matrix to be used in multilayer matrix method analysis.

With the ideal system well modeled, we next address the contribution of random and systematic error. First, Gaussian noise of standard deviation 0.03 Å (which was found to be typical for our system) [92] was then added to the fringe data to simulate peak wavelength uncertainty. To add type 1 systematic error, we analyzed the substrate thickness and dispersion with the refractive index fixed at a deliberately incorrect value. Type 2 error is ignored based on the assumption that clean substrates were used. Finally, type 3 systematic error was induced by incorporating the variation in the fluid refractive index due to the

adsorbed polymer layer. The simulated data was analyzed with the middle layer treated as a single

homogeneous layer (bulk water) using the new analytical method. Figure 2.5 shows the mean refractive

index profile before (red circles) and after (blue x symbols) the simulated data (simulated using equations

7-9 and the 3-slab method) was analyzed with the methods described above, along with the mean

refractive index used to generate the data (black line). The corrected data is well described by the error-

free profile, indicating that correction method effectively removed the systematic errors even when

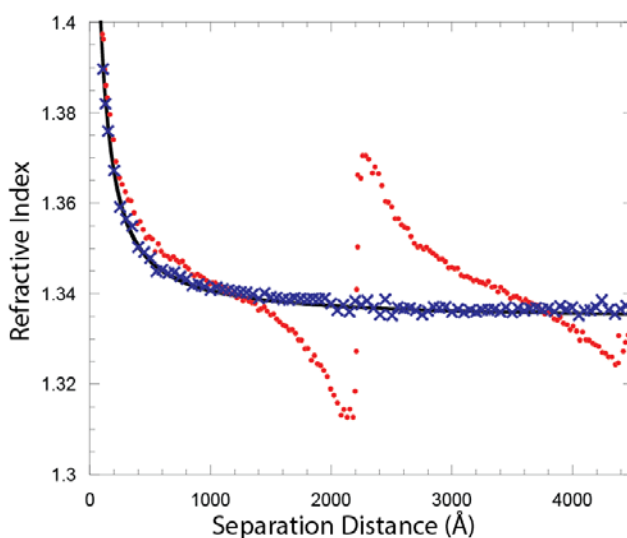including realistic random error.

Figure 2.5 Plot of realistic simulated refractive index data of a system with an increasing refractive index with confinement at low separation distances (simulated using Eq 2.7), analyzed with a constant refractive index at each separation distance (red circles), and mean refractive index found after determining substrate and transition layer properties using the methods described (blue ×). Actual mean refractive index is shown by the solid line.

The transition layer found had a $\Delta\Omega$ value of 3.4 ± 0.2 Å, and the $\Delta\Omega$ value used for the simulation

was 3.32 Å, which are in excellent agreement. At the input refractive index of 1.5, the $\Delta\Omega$ corresponds to

a dry film thickness of 20 ± 1 Å, which is the accuracy typically expected from SFA measurements. Thus,

the analytical method is theoretically feasible. To determine the uncertainty of the transition layer $\Delta\Omega$

from the simulation, which arises as a result of random error in the fringe wavelengths, the same data

was reanalyzed 100 times with new random Gaussian error added before each analysis, and the standard deviation was taken of the results.

Experimental Results and Discussion

As a direct demonstration of this analytical technique, we measured the optical thickness of aqueous PEI adsorbed onto mica using the method described (without contacting the adsorbed PEI surfaces), and compared this to highly compressed contact measurements of the PEI coated surfaces. The $\Delta\Omega$ of the transition layer was determined to be 1.9 ± 0.2 Å from the average of four experiments, and this result corresponds to a measure of the $\Delta\Omega$ value of the adsorbed polymer on each surface. The uncertainty of transition layer measurement was determined using a block bootstrap analysis, which is appropriate if the data is fine-grain enough to exhibit the systematic features after resampling. The data was split into blocks of three data points and one data point from each block was randomly selected, and the set was analyzed. This was repeated 20 times for each experiment, and the uncertainty on the optical thickness of the transition layer was taken as the standard deviation. The value found was the same as the standard deviation of the optical thickness data.

The thickness and refractive index of the compressed polymer layer were 9.9 ± 0.2 Å and 1.520 ± 0.007, respectively, giving $\Delta\Omega$ = 1.84 ± 0.2 Å, which is within error of the analyzed profile measurements. The uncertainty in this measurement was determined using a Monte-Carlo error analysis as described by Kienle et al [92]. The high refractive index of this measurement suggests that nearly all of the water was displaced from the polymer under compression, making this comparable to a dry thickness. Given the bulk value for branched PEI of 1.53, we can estimate the thickness of the compressed polymer from the transition layer $\Delta\Omega$ using Eq 2.1, giving a compressed thickness of 10.5 ± 0.8 Å. This demonstrates that the mass of the polymer between the surfaces is conserved through confinement and shows that the analytical method described can achieve the accuracy expected of SFA experiments. The grafting density was calculated from the result to be 1.07 ± 0.08 mg/m^2, and the hydrodynamic thickness was found to be

around 35 Å from force profile results. Therefore, the molecules have a flat conformation as expected for

a polycation solution of low ionic strength on a negatively charged surface, with loops and tails extending
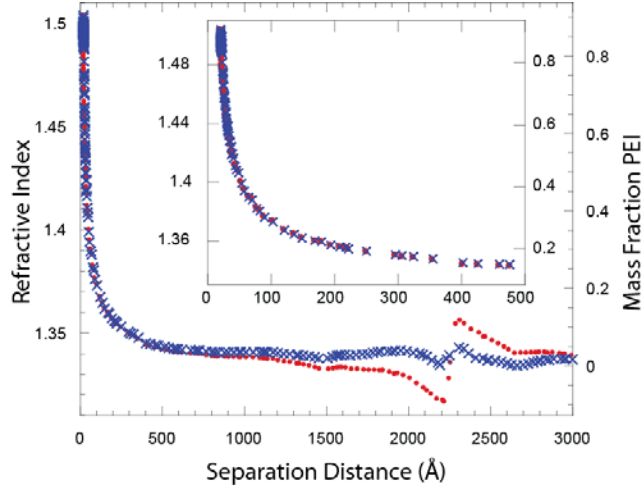
out to 35 Å.

Figure 2.6 Plot of mean refractive index profile data analyzed without transition layer (red circles) and the mean refractive index profile found using the transition layer analysis (blue ×). The inset is a close up of the profiles at low separation distance. Mass fraction of PEI is plotted on the right axis using Eq. 2.10.

The refractive index profile for one example data set is shown in Figure 2.6.   The plot

demonstrates that the analysis was effective in removing type 3 error. For this particular data set, it was

not necessary to correct for type 1 error. The right axis indicates the mass fraction of the polymer which

was approximated using

$$x_{PEI} = \frac{n_{measured} - (1 - x_{PEI}) n_{water}}{n_{PEI}} \qquad (2.10)$$

where x_{PEI} is the volume fraction of the PEI, $n_{measured}$ is the mean refractive index in the cavity and n_{PEI} and

n_{water} are the bulk refractive indices of PEI and water.

The corrected result in figure 2.6 still shows a small oscillation at the sensitivity antinode. The

residual perturbation is within the expected uncertainty at these separations distances (see Figure 2.2).

However, this is clearly a systematic effect that could not be eliminated using transition layer (see SI for

information on handling alternative sources of systematic errors). We attribute this small error to secondary fringes resulting from a mismatched refractive index of the glue layer and glass disc, which can occasionally cause low amplitude interference to the refractive index data depending on the thickness of the glue. The heightened sensitivity at the sensitivity antinode amplifies this glue-effect resulting in oscillations that cannot be removed with the method described.

Conclusions

An analytical method which can determine specific substrate and film or heterogeneous fluid properties near a surface without confinement of the fluid or contacting the surfaces was described in the context of interferometric measurements as utilized in the SFA. The method works by analyzing data at multiple separation distances beyond confinement and modeling variable refractive index as multiple surface layers, which enables extraction of the film thickness and refractive index. The method was demonstrated using realistic simulated data with added error of a magnitude similar to experimental error in typical SFA experiments. The analyzed simulation returned the expected values with excellent error bounds. Physical experiments on a polymer film of PEI adsorbed from water were also analyzed as a demonstration of the technique. The analysis returned a film thickness of 10.5 ± 0.8 Å with a refractive index of 1.52, which is within error of the compressed film measurement of 9.9 ± 0.2 Å for the thickness, with a refractive index of 1.520 ± 0.007. The technique provides a way of determining film properties while avoiding potentially damaging or film-altering contact. It can also be used to measure the optical thickness of depletion layers or similar films that do not exist when the surfaces are in contact. Finally, strategies to eliminate the effects of systematic and random error at various separation distances in SFA apparatus experiments were described and demonstrated in detail.

Acknowledgement

Chapter III

Analyzing Refractive Index Profiles of Confined Fluids by Interferometry Part II: Multilayer and Asymmetric Systems

Daniel F. Kienle and Tonya L. Kuhl*
Department of Chemical Engineering and Materials Science, University of California Davis, 95616, USA
*Corresponding author. E-mail: tlkuhl@ucdavis.edu

Abstract

Methods for determining the substrate properties and the optical thickness of thin films or any variation in the refractive index of a fluid or film near a surface for unknown 5-layer symmetric and 3-layer asymmetric interferometers are presented. Both systems can be fully resolved without any known layer properties and without contact or confining the films. The method was tested using realistic simulated interferometer data, and was found to consistently yield accurate values for all desired properties. The method was experimentally validated through analysis of an asymmetric three layer interferometer system of linear polyethyleneimine (LPEI) adsorbed onto mica substrates of differing thickness and identical refractive index. The results were in excellent agreement with the dry polymer film properties measured using conventional SFA contact measurements. More complicated systems were also evaluated for feasibility, and any additional parameter specifications required for analysis were determined. The utility of this method is broad, as a single experiment in a laboratory setting can independently provide non-contact film properties and the effects of confinement on the film structure, which can be correlated to a simultaneously measured interaction force profile.

Introduction

The surface force apparatus (SFA), which has primarily been used to measure interaction force profiles, can also be used to measure refractive index profiles of fluids confined between surfaces [38, 74-78, 99]. While the measurements are limited to mean refractive index profiles, and are lower resolution than alternative techniques used for evaluating liquid properties near a solid surface such as X-ray and neutron scattering [67] and recently nanoultrasonics [100], the coupling of refractive index with force measurements, and the ability to confine the fluid, present advantages over other methods. With these abilities, any structurally induced interaction between surfaces can be observed. Additionally, the method is convenient because it uses the visible spectrum and will work over a wide range of geometries and materials.

The SFA uses multiple beam interferometry (MBI) to measure the separation distance between two surfaces and the refractive index of the medium separating those surfaces (central medium). Measurements are taken in the SFA by directing collimated white light through an etalon, generating intensity peaks at discrete wavelengths called fringes of equal chromatic order (FECO) [91]. Spectrographic measurements allow the wavelength of the FECO to be determined via peak fitting. FECO simulated using the multilayer matrix method [47] are fit to the measured FECO to determine optical properties of the system such as layer thickness and refractive index [92].

Recently, we developed a method based on the SFA for determining the variation in the fluid refractive index near a surface without confining or contacting the surfaces [99]. The approach can be used to probe surface effects on a fluid's structure independent of the effect of confinement, which was previously not possible. This capability could be extremely valuable for deducing any changes in the structure of a fluid upon confinement. Such measurements have only seldom been performed using very specialized equipment [68-71, 73, 101] and were incapable of measuring interaction forces. Moreover, characterizing thin films without contact or confinement is advantageous for fragile deposited film,

polymer brushes whose distributions change with confinement, or other systems with concentration and density gradients.

More specifically, the analysis developed in this work is capable of determining the change in optical thickness $(\Delta\Omega)$[b] from the bulk of a fluid or film with variable refractive index near the surface, as well as the specific substrate properties of the system. As described previously [99] (see chapter 2), the method was originally developed for analyzing symmetric, 3-layer interferometers which are the most optically simple system studied using the SFA. The technique requires a spectrum taken in the absence of the central medium (see Figure 3.1) when the surfaces are in contact (referred to as the FECO contact spectrum), along with a sequence of spectra with the central medium present taken at different inter-surface separation distances that must include values ranging from 100 nm to 300 nm (referred to as the FECO profile spectra). Simply put, the analysis corrects systematic error in the refractive index profile by determining the substrate properties and the optical thickness of a 'transition layer' (see Figure 3.1) at the substrate surface (incorporated to compensate for the variations in the refractive index of the "central medium" near (or at) the surface). This is a powerful tool because the optical properties of an entirely unspecified 3-layer symmetric interferometer can be fully determined without contact or confinement. Furthermore, the change in the optical thickness is analogous to the total increase or decrease in mass density, and the data from the transition layer analysis can be used to determine the refractive index profile or corresponding mass density profile over a long range of separation distances.

The technique henceforth referred to as the refractive index profile correction (RIPC) method, is currently limited to simple 3-layer symmetric systems. As more complex systems are frequently of interest, the method is extended here to enable analysis of symmetric 5-layer and asymmetric 3-layer interferometers. For example, surfaces are often functionalized with materials to tailor properties. If the

---

[b] Optical thickness refers to the thickness times the refractive index. The change in optical thickness is defined as $\Delta\Omega = \int_0^\infty (n_{local}(z) - n_{bulk})dz$ where n_{local}, n_{bulk} and z are the local and bulk refractive indices and the normal distance away from an interface, respectively [99].

properties of the material can be determined in situ by independently measuring the substrate and deposited film properties without reorienting the sample or optics, extension of the 3-layer RIPC method only requires the inclusion of an additional known layer in the analysis. In many cases, however, the layers cannot be removed or deposited in situ without moving the sample. For example, hydrophobic surfaces are difficult to repeatably deposit directly onto mica with high stability, so more optically complicated systems are sometimes implemented, such as the addition of layers to link the hydrophobic molecules to mica [102], or the use of alternative substrates. Some other commonly studied examples are silica layers deposited on mica, [32, 103] or thick and inert polymer films such as PDMS. When the additional layers cannot be reliably removed, the current RIPC method cannot be used.
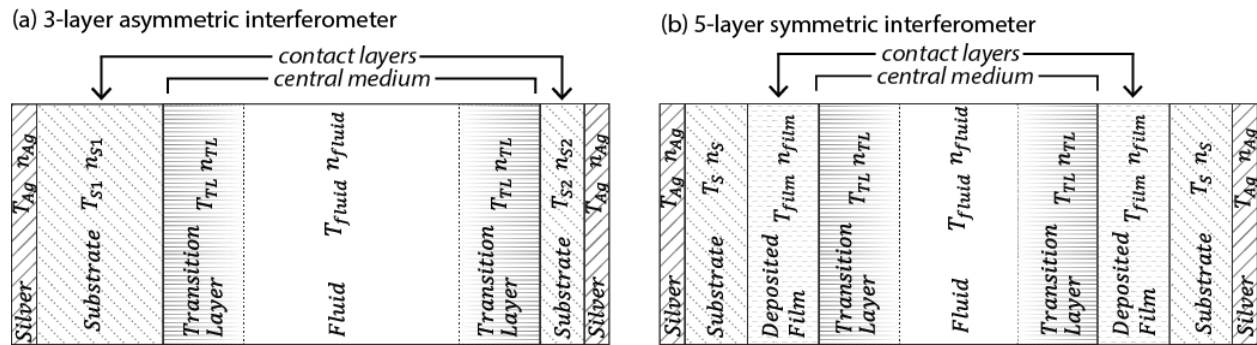
(a) 3-layer asymmetric interferometer

contact layers
central medium

Silver T_{Ag} n_{Ag} | Substrate T_{S1} n_{S1} | Transition Layer T_{TL} n_{TL} | Fluid T_{fluid} n_{fluid} | Transition Layer T_{TL} n_{TL} | Substrate T_{S2} n_{S2} | Silver T_{Ag} n_{Ag}

(b) 5-layer symmetric interferometer

contact layers
central medium

Silver T_{Ag} n_{Ag} | Substrate T_S n_S | Deposited Film T_{film} n_{film} | Transition Layer T_{TL} n_{TL} | Fluid T_{fluid} n_{fluid} | Transition Layer T_{TL} n_{TL} | Deposited Film T_{film} n_{film} | Substrate T_S n_S | Silver T_{Ag} n_{Ag}

Figure 3.1 Illustration of the interferometers that the extended RIPC method can analyze. T refers to the thickness and n refers to the refractive index of each layer. The transition layer refers to a region of variable refractive index from the bulk medium.

It is also occasionally necessary to use substrates with non-uniform thickness, which results in opposing substrates with differing thicknesses within the etalon.   For example, mica substrates are sometimes re-cleaved just before being mounted in the SFA box to remove any contamination that may have occurred during preparation [82]. This re-cleaving will result in substrates with different thicknesses. Another example that we are currently working on is the use of silica substrates that are made from blown quartz bubbles [104-106] which can have considerable variation in the thickness. These systems yield asymmetric 3-layer interferometers and cannot be analyzed using the current RIPC method. Indeed, many

systems where information on the confined fluid structure would be valuable are difficult to study due to the current limitations in the RIPC method.

In this work, we have developed algorithms for extending the RIPC method to 3-layer asymmetric interferometers with substrates of the same refractive index (here on referred to as 3-layer asymmetric) and 5-layer symmetric interferometers, as depicted in Figure 3.1a and b respectively. Using the methods developed here, both of these systems can be fully specified without any prerequisite known properties.[c] We demonstrate the efficacy of the algorithms by applying them to realistic simulated data and by analyzing data from an experiment with a 3-layer asymmetric interferometer consisting of mica substrates of different thickness, with an adsorbed polymer thin film of polyethyleneimine in water. Finally, we assess what would be required to further extend the RIPC method to even more complicated interferometers.

Experimental Section

The analytical method described below is applied to an example experimental system as a demonstration. The system consists of mica substrates of asymmetric thicknesses and identical refractive indices, with an adsorbing polyelectrolyte solution between them. The mica was cleaved and selected from adjacent regions of different uniform thickness to ensure that any differences in the refractive indices were negligible. The selected mica was cut and silvered on the back side as described previously. The mica was glued silver-side down onto two plano-convex cylindrical BaLF4 glass lenses, using refractive index matched EPON 1002F epoxy resin as a hot melt glue. The samples were rinsed in 18 MΩ-cm water, blown dry with nitrogen and mounted in the SFA in a cross-cylinder orientation forming an interferometer.

---

[c]The silver layers on the outsides of the interferometer which are measured during deposition do need to be specified prior to analysis. However, the multilayer matrix analysis is much less sensitive to error in the silver layer properties than to other layers in the interferometer. An acceptable error in the silver layer properties is that which results in FECO wavelength deviations below the typical noise threshold of 0.03 Å. Simulations show that the acceptable silver thickness error in Angstroms is around $\pm$ (1.2 × 10-4)$T_{substrate}$, where $T_{substrate}$ is the substrate thickness in Angstroms.

The SFA and mounted mica surfaces were further dried by purging dry nitrogen for 15 min. Measurements were taken by directing collimated white light from a tungsten halogen bulb through the interferometer, generating FECO which were measured using a ¾ meter spectrometer. The FECO contact spectrum was recorded with the substrates in contact. The mica surfaces were then separated and several drops of an aqueous solution consisting of 100 µg/mL LPEI hydrochloride salt (molecular weight of 20kDa and polydispersity index of 1.2 purchased from Sigma-Aldrich) and 0.5 mM NaNO$_3$ (99.995% pure from Sigma-Aldrich) in 18 MΩ-cm water were placed between the substrates and allowed to equilibrate for 30 min. At this point FECO profile spectra were collected while driving the lower surface, which was mounted on a spring, at constant step sizes. The interaction force was also measured at each step by determining the spring deflection, which was used to determine the force based on Hook's Law. Finally, the samples were rinsed with pure water, dried and put into contact where another spectrum was recorded for an independent measurement of the LPEI film thickness and refractive index.

Systematic Errors

Before describing modification to the RIPC method, it is important to understand the systematic errors on which the method is based.   In short, analysis of measurements with incorrect values for system parameters yield well-understood systematic errors. The RIPC analysis iteratively determines the correct system parameters by minimizing these systematic errors. The cause and effects of these errors have been described in greater detail previously [99] (see chapter 2) and are reviewed here. One error arises from having an accurate contact spectrum with a false solution for the substrate properties, which is referred to as a type 1 error. This error is essentially unavoidable, because the solution of the MBI FECO wavelengths is extremely sensitive to error when attempting to determine all of the substrate properties simultaneously. Even when a substrate property is precisely known, the substrate can have different apparent properties based on the optics of the system [92]. Type 2 error occurs when the substrate contact spectrum is not accurate as a result of contamination, deformation or rough interfaces. Generally,

type 2 error can be ignored if samples are prepared carefully [84] and will not be discussed further. Type 3 error is an error that occurs when the central medium (see Figure 3.1) has a refractive index that varies with distance away from the substrates but is treated as though it has a constant or bulk value. In this case, even if the mean refractive index of the central medium is allowed to vary when analyzing the FECO profile spectrum at each separation distance, the local changes in the refractive index are not accounted for, resulting in type 3 error.

The effects of each of these errors depends on the interferometer. For the simplest system of a symmetric 3-layer interferometer, type 1 error causes a constant offset in the refractive index profile (Figure 3.2a, red dashed line), and type 3 error causes oscillations in the refractive index profile (Figure 3.2b, red dotted line). A feature of these oscillations that is important for the RIPC analysis is the appearance of the sensitivity nodes and sensitivity antinodes as indicated in Figure 3.2b. The refractive index at the sensitivity nodes is insensitive to type 3 error, while the amplitude of the sensitivity antinodes is insensitive to type 1 error. Therefore, type 1 and type 3 errors can be corrected independently using the refractive index values around these nodes to yield substrate and transition layer properties and an accurate mean refractive index profile. The methods for analyzing the FECO data and these errors when incorrect parameters are used are what enable accurate parameter values to be extracted from the data.

The 3-layer interferometer with asymmetric substrate thicknesses is affected in exactly the same way that the symmetric system is for both type 1 and type 3 error. Complications to the analysis do arise from the asymmetry of the system if the thicknesses of both substrates are unknown, which is often the case for SFA experiment. The method used to handle this situation is described in the next section.
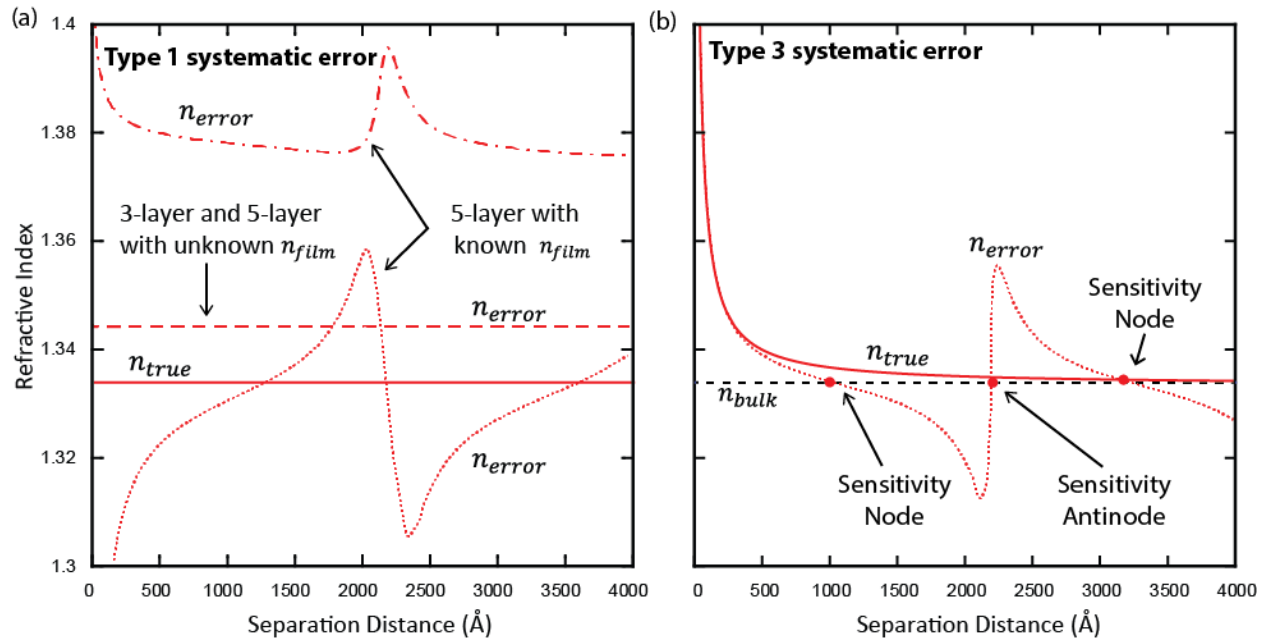
Figure 3.1 Plots of refractive index profiles (fitted mean central medium refractive index vs. the fitted separation distance of the contact layers) due to common systematic errors for different interferometer systems. The errors lead to obviously incorrect refractive index profiles. Correct values for thickness and refractive index are determined precisely through correction of these errors. (a) Type 1 error for the 3-layer system and 5-layer system with unknown deposited layer refractive index (n_{film}) which causes a constant offset (dashed red line) from the true refractive index profile (n_{true}, solid red line), and type 1 error for the 5-layer system with known n_{film} which causes both an offset and oscillations in the refractive index profile (red dotted and dot-dashed lines which are a result of inaccurate substrate refractive indices above and below the true substrate refractive index, respectively). (b) Type 3 error for all systems described, which causes an oscillatory refractive index profile (dotted red line) about the true refractive index profile (solid red line). The sensitivity node and antinode are indicated by red dots, where refractive index profile with type 3 error is equal to the bulk refractive index. The profiles shown are for a positive $\Delta\Omega$. The profile corresponding to a negative $\Delta\Omega$ would be approximately equivalent to n_{error} mirrored about the bulk refractive index.

The effects of systematic errors can be different for the 5-layer interferometer depending on whether the refractive index of the deposited film is fixed or allowed to vary when analyzing the contact spectrum, which in this case is taken when the deposited layers are in contact. In both cases type 3 error has the same effect as with a 3-layer interferometer. If the deposited layer refractive index is unknown and varied, type 1 error will result in a constant offset of the refractive index as with a 3-layer interferometer. If the deposited layer refractive index is fixed at a precisely known value, type 1 error will result in both an offset of the refractive index and perturbations of the refractive index near the sensitivity antinode as shown in Figure 3.2a (red dotted line and dot-dashed line), which means that type 1 and type 3 error cannot be independently corrected for this system. In this case, type 1 error takes two forms

48

depending on whether the inaccurate substrate refractive index used to analyze the contact is above (Figure 3.2a, dotted red line) or below (Figure 3.2a, dot-dashed red line) the true substrate refractive index. The method used to analyze these oscillatory type 1 errors is the same regardless of the direction of the inaccuracy in the substrate refractive index. The necessary modifications to the analytical method will be described in the next section.

Analytical Methods

The RIPC method follows two fundamental steps for any system which uses global variables to correct type 1 and type 3 errors. Here, a global variable refers to an unknown property that is constant, such as the properties of a solid substrate or deposited film, or any film not contained in the central medium. The first step is to vary at least one global variable (other than the Cauchy dispersion coefficient - see Eq. 1.1) with the constraint that the contact properties are a solution to the contact spectrum. The contact spectrum is reevaluated at each value of the globally varied property, and the results are used to analyze the profile data (FECO wavelengths at different separation distances that make up the FECO profile spectra). The correction is achieved by setting the central medium refractive index at the sensitivity nodes ($n_{node,I}$ where the subscript i distinguishes different sensitivity nodes in a single refractive index profile) equal to bulk (n_{bulk}) thereby minimizing the fitting argument given by

$$arg = \Sigma(n_{node,i} - n_{bulk})^2 \tag{3.1}$$

and specifying any unknown properties included in the contact spectrum. It should be noted that only the thick substrate layer is treated with a dispersive refractive index given by Eq. 1.1 because the effects of dispersion are negligible for thinner films.

The second step is to globally vary the transition layer optical thickness to correct type 3 error by minimizing the standard deviation of the central medium refractive index near the sensitivity antinodes. There are some variations to how these steps are implemented depending on the interferometer being analyzed. The algorithms described in this section are shown schematically in the supporting information.

49

The 3-layer system with asymmetric substrate thickness can be analyzed with a straight forward extension of the 3-layer symmetric system. The difference between the two systems is that the thickness of the individual substrate layers cannot be determined from the contact spectrum alone for the asymmetric system. Instead, the contact spectrum is analyzed with the substrate refractive index fixed at an estimate to return the dispersion and combined thickness. Then the individual substrate thicknesses can be determined from the profile data. One substrate thickness is varied along with the thickness and refractive index of the central medium, and the other thickness is set to the difference between the combined substrate thickness and the varied substrate thickness. The average of the individual substrate thicknesses throughout the profile give an accurate thickness for the individual substrates. It should be noted that the order of the substrates in the interferometer does not matter, so the search window of the varied thickness can be reduced to only above or below half the total thickness to save time.

Subsequently, type 1 error is corrected as described above by varying the substrate refractive index. The sensitivity nodes can be determined using the same methods as described for a 3-layer symmetric interferometer [99]. A complication arises while correcting type 1 error from the need to determine the individual substrate thicknesses at each iteration, which are required to analyze the profile data. Conveniently, the ratio between the substrate thicknesses is approximately constant when the total thickness is determined with different substrate refractive indices. This allows one to define a close guess of the specific substrate thicknesses using the combined thickness which can be determined when reanalyzing the contact spectrum at each iteration. The profile spectra corresponding to the sensitivity node data points (sensitivity node spectra) are analyzed as described for the profile spectra in the previous paragraph, using the redefined contact properties and a much narrower search window for the substrate thickness (e.g. from 40,000 Å to 200 Å which includes only one minimum). This returns the accurate individual substrate thicknesses and the n_{node} values required to define the fitting argument for type 1 error correction. Type 3 error is corrected using the second step of the analysis without any modifications.

There are two algorithms for doing an RIPC analysis of 5-layer interferometers depending on whether the refractive index of the deposited film is constant or variable. When the refractive index is constant, type 1 and type 3 error are interdependent, so the contact properties and the transition layer can be determined simultaneously by minimizing the sum squared error in the refractive index around the sensitivity antinode as in the second step of the analysis. More specifically, the substrate refractive index and transition layer thickness are globally varied simultaneously. At each iteration, the contact spectrum is analyzed using the new substrate refractive index to return the substrate thickness and dispersion and the deposited layer thickness. These are then used with the transition layer properties to find the refractive index profile around the sensitivity antinode, from which the sum-squared error can be calculated. The fitting argument is iteratively minimized to return the transition layer and substrate properties.

When the refractive index is unknown (with or without known thickness), type 1 and type 3 errors must be corrected separately, as with a 3-layer interferometer. The location of the sensitivity nodes can be determined using the same method as with a 3-layer interferometer if the profile measurement can be taken at contact (including the transition layers) by finding the FECO set where the fringe wavelengths most closely bisect the contact fringes of the same order and the next lowest order. This condition may be represented as

$$\{\lambda_{node}\} = \underset{\{\lambda(D)\}}{\mathrm{argmin}} \sum_m \left| \lambda_m(D) - \frac{\lambda_{m-1}^0 + \lambda_m^0}{2} \right| \qquad (3.2)$$

where $\{\lambda_{node}\}$ is the set of fringe wavelengths from the spectrum at the sensitivity node, $\{\lambda(D)\}$ represents the fringe wavelength set as a function of separation distance D (FECO from the profile spectra), m is the fringe order, $\lambda_m(D)$ is the fringe of order m in the set $\{\lambda(D)\}$ and λ_m^0 is the fringe of order m in the set of fringes measured in contact.

If non-contact measurement is required, the location of a sensitivity node can be approximated if the refractive index profile is analyzed without correction, using

$$\{\lambda_{node}\} = \left\{\lambda\left(\frac{D_{antinode}}{2}\right)\right\} \qquad (3.3)$$

where $D_{antinode}$ is the separation distance where the antinode occurs. For these methods, $\{\lambda_{node}\}$ will need to be set at the measured spectrum that most closely satisfies Eq 3.2 or 3.3. These methods are universal to all interferometers. $D_{antinode}$ can be defined as the separation distance at the maximum absolute slope or the maximum in the refractive index profile between separation distances of 1000 and 3000 Å:

$$D_{antinode} = \underset{D\in[1000,3000]}{\mathrm{argmax}} \left|\frac{dn}{dD}\right| = \underset{D\in[1000,3000]}{\mathrm{argmin}} \sigma_{profile} \qquad (3.4)$$

If available, it can also be defined at the minimum fitting error of the profile measurements ($\sigma_{profile}$), when fit with the refractive index fixed at bulk which is useful with noisy dn/dD. If a second sensitivity node is desired, $D_{antinode}$ can be replaced in Eq 3.4 by ($D_{antinode,1}+ D_{antinode,2}$), where the second antinode is found using the same method except between separation distances of 3000 and 5000 Å.

In many cases, the layers that are deposited on the substrate are very thin and may not contribute significantly to the optics. This raises the question of how thick a layer can be before it has an important effect on the RIPC results, as neglecting a layer can dramatically simplify analysis. Simulations of a system with an input transition layer and a wide range of substrate and deposited layer properties were analyzed as a 3-layer system in an attempt to estimate the error on the transition layer. It was found that the error in transition layer thickness (δ) approximately follows

$$\delta \approx \frac{4T_{layer}}{n_{tl}^2}\left(n_{layer}^2 - n_{substrate}^2\right) \qquad (3.5)$$

within ± 2 Å. The error that results from ignoring a thin layer is steeper than would be predicted based on optical thicknesses alone, and would only be acceptable for systems where the layer and substrate refractive index are similar and the film is very thin.

Simulation

The RIPC method is demonstrated by analyzing simulated FECO data {λ} for an asymmetric 3-layer and a symmetric 5-layer interferometer as described above, where the simulated contact and profile spectra have added random error with a standard deviation of 0.03 Å in wavelength. For both systems, the central media is defined with a non-constant local refractive index (n_{local}) extending from either surface:

$$n_{local} = \begin{cases} (1.5 - 1.334)e^{-z/10} + 1.334, & z \leq 40 \\ 1.334, & z > 40 \end{cases} \qquad (3.6)$$

where z is the distance from the surface. The refractive index profile is the solid line in Figure 3.3. The simulation of these data is accomplished using the methods described previously [99] (see chapter 2) where the refractive index is truncated to reduce computation time.

The variation in the refractive index induces type 3 error with a theoretical transition layer ΔΩ of 9.81 Å, and the use of an incorrect substrate refractive index induces type 1 error. Each of the systems described was analyzed with the RIPC method 50 times using a Monte Carlo type error analysis, where new random error added each iteration to determine the uncertainty in each of the properties being varied. Figure 3.3 shows the results of one iteration for (a) the 3-layer asymmetric system and (b) the 5-layer symmetric system, with the refractive index of the deposited film fixed and the thickness of the deposited film varied. The corrected profile (blue x) is fit well by the input mean refractive index profile (black line), indicating that type 1 and type 3 errors were successfully removed from the initial erroneous profile (red circles).
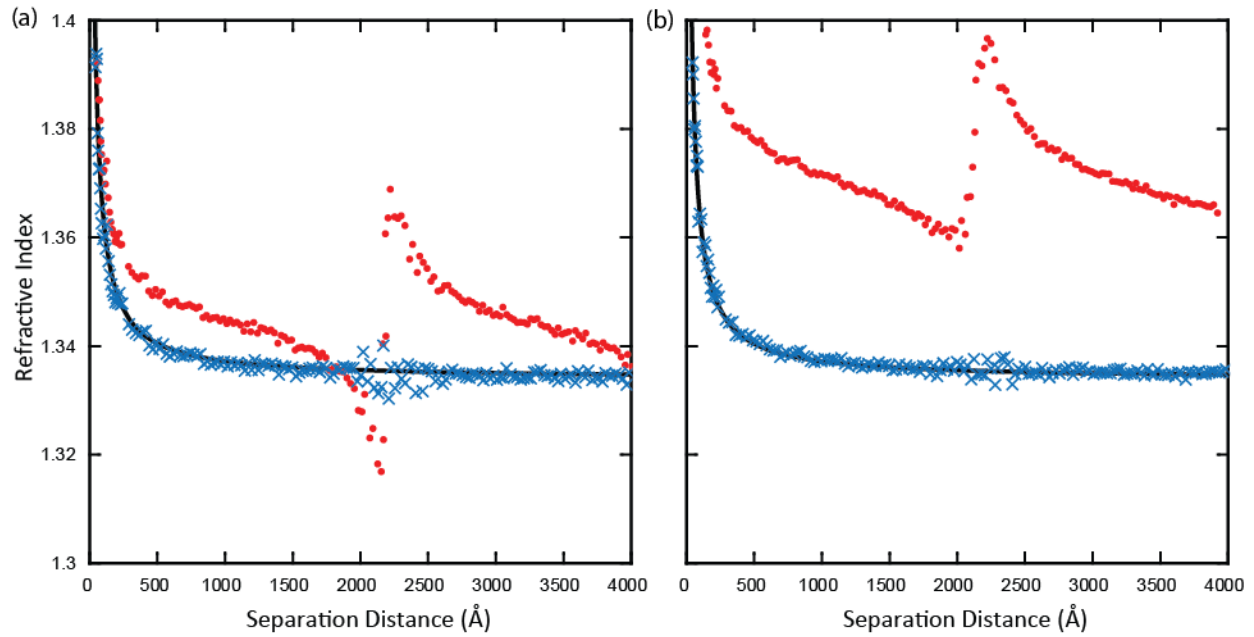
Figure 3.3 Plot of simulated mean refractive index data with added type 1, type 3 and random error (red circles), along with the results after correction using the RIPC method (blue ×) and the actual mean refractive index (black line). Results are for a 3-layer interferometer with substrates of differing thickness (a), and a 5-layer interferometer with a fixed refractive index, and varied thickness of the deposited layer (b).

Table 3.1 shows the values found for each of the properties determined from the analysis, along with the input parameters.   For all of the systems, every property was within uncertainty of the input value. The transition layer thickness had an uncertainty less than ± 1 Å which is consistent with the accuracy expected of SFA thickness measurements.   The other thicknesses determined had larger uncertainties, especially in the 5-layer interferometer where the refractive index and thickness were both being varied, as is expected due to the additional variables. The primary purpose of this method is to determine accurate refractive index profiles and the properties of the transition layer, so the higher uncertainty in the other properties such as substrate thickness is acceptable.

Table 3.1 Input simulation properties and results of a Monte-Carlo error analysis using RIPC analytical method for a 3-layer asymmetric interferometer and a 5-layer symmetric interferometer.

3-layer asymmetric interferometer	$T_{substrate1}$ (Å)	$T_{substrate2}$ (Å)	$n_{substrate}$	Substrate dispersion $(10^5 Å^2)$	$\Delta\Omega_{TL}$ (Å)	T_{TL} (Å) at $n_{TL} = 1.5$
Input values	55,000	45,000	1.447	3.65	1.63	9.82
Results	54,990 ± 20	44,990 ± 10	1.4473 ± 0.0004	3.651 ± 0.006	1.69 ± 0.06	10.2 ± 0.4

5-layer symmetric interferometer	$T_{substrate}$ (Å)	$n_{substrate}$	Substrate dispersion $(10^5 Å^2)$	T_{film} (Å)	n_{film}	$\Delta\Omega_{TL}$	T_{TL} (Å) at $n_{TL} = 1.5$
Input values	50,000	1.575	4.85	500	1.458	1.63	9.82
n_{film} fixed T_{film} varied	50,000 ± 10	1.5749 ± 0.0002	4.847 ± 0.008	500 ± 8	--	1.56 ± 0.09	9.6 ± 0.3
n_{film} varied T_{film} fixed	50,000 ± 20	1.5752 ± 0.0007	4.849 ± 0.008	--	1.4582 ± 0.0005	1.6 ± 0.1	9.8 ± 0.7
n_{film} and T_{film} varied	50,000 ± 100	1.575 ± 0.004	4.85 ± 0.02	500 ± 9	1.458 ± 0.004	1.6 ± 0.1	9.8 ± 0.7

Experimental Results and Discussion

The method is further demonstrated by determining the optical thickness of a linear polyethyleneimine (LPEI) film adsorbed from water onto the surface of mica substrates with asymmetric thicknesses and identical refractive index values, using the non-contact analysis described for 3-layer asymmetric systems. The results are compared to the independently measured dry polymer film thickness. The value and uncertainty found for all search parameters used in the RIPC analysis of seven data sets are given in Table 3.2. The corresponding corrected and uncorrected refractive index profiles for all seven experiments are shown in Figure 3.4a, and demonstrate that type 1 and type 3 error were reduced to below random error. A bootstrap analysis was performed on the data to determine if uncertainty on any individual transition layer exceeded the standard deviation of the experimental data. To do this, the profile data was split into blocks of three data points and resampled by randomly selecting a point from each block and analyzing the selection. This was repeated for 20 iterations. The uncertainty of the reanalyzed substrate thickness was slightly greater than the experimental error at ± 15 Å over ± 5 Å while the uncertainty of the $\Delta\Omega$ was below the experimental error at ± 0.05 Å. The greater of the bootstrap or experimental uncertainties are reported as the uncertainties in Table 3.2.

The dry LPEI films were determined to have a thickness of 15.8 ± 0.1 Å and a refractive index of 1.538 ± 0.007. These values are in excellent agreement with the non-contact RIPC thickness of 15.9 ± 0.9 Å and the refractive index of branched PEI of 1.529 (we were unable to find values for linear PEI). Based on the dry PEI film properties, the adsorbed amount of PEI on the mica surface is 1.7 ± 0.1 mg/m^2.

Table 3.2 Values and uncertainties determined for all search parameters when applying the 3-layer asymmetric RIPC method to an experimental system composed of linear PEI adsorbed onto mica substrates of asymmetric thicknesses and identical refractive index values.

	$T_{substrate1}$ (Å)	$T_{substrate2}$ (Å)	$n_{substrate}$	Substrate dispersion (10^5 Å^2)	$\Delta\Omega_{TL}$ (Å)	T_{TL} (Å) at $n_{TL} = 1.54$
Experiment Results	51061 ± 15	45632 ± 15	1.5823 ± 0.0002	5.1630 ± 0.0006	**3.1 ± 0.2**	**15.9 ± 0.9**

The corrected refractive index profile shown in Figure 3.4a (blue x) represents the weighted average of refractive index results across the central medium including the transition layers (i.e. PEI film - solution - PEI film), as a function of separation distance. Thus, the mean refractive index increased as the solution was displaced and the PEI film, with a higher refractive index, occupied a larger fraction of the central medium thickness. An illustration of what the local refractive index profile of an individual film may look like is plotted in the inset (dashed line) with the steep profile to indicate that the film is tightly bound to the mica surface. The refractive index profile does not deviate from the expected value calculated as the weighted average of the transition layers and water refractive indices (solid black line). This is an indication that the mass of the adsorbed film was conserved during compression and contact as expected for a tightly bound film.

The force profile data is displayed in Figure 3.4b. The results show a repulsive double layer force and an attractive force at a length scale consistent with Van der Waals attraction. The force profile indicates that the LPEI forms a tightly bound, compact layer, without steric interactions from polymer loops or tails extending into the solution. A schematic is shown in the inset of Figure 3.4b. A pure exponential fit at large separations was used to determine the Debye length of 130 ± 8 Å and corresponding counterion concentration of 0.55 ± 0.07 mM. As expected, the electrolyte concentration is higher than the concentration of $NaNO_3$ in solution, due to the Cl^- counterion of LPEI hydrochloride salt. If the LPEI fully dissociated, the concentration of Cl^- would be ~1.8 mM, based on the 40-50% Cl^- contribution to the molecular mass of the LPEI. The lower counterion concentration indicates that only 3.8% of the LPEI is dissociated and charged.

The force profiles over all separations were fit with Derjaguin, Landau, Verwey, and Overbeek (DLVO) theory using an origin of charge and Van der Waals plane at a separation of 31.6 Å (LPEI film contact). The double layer forces were modeled using the Poisson-Boltzmann equation with constant charge boundary conditions and the fitted ion concentration of 0.55 mM. The non-retarded Van der

Waals interaction was modeled using a Hamaker constant of 1.92×10^{-20} for the LPEI film based on Lifshitz theory with a dielectric constant of 3.8 and the measured refractive index of 1.538. The best fit indicates a surface charge density of 2.38 mC/m^2 and a corresponding surface potential of 38.7 mV. The percent of charged LPEI monomers at the surface estimated based on this surface charge and the adsorbed amount of 1.7 mg/m^2 is 0.1%. This is considerably lower than the estimate based on the 3.8% charged LPEI from the counterion concentration, which is not unexpected as a portion of the positively charged LPEI will be neutralized by the negatively charged sites on the mica surface. Considering that there are about six amine groups adsorbed per negatively charged site in mica (which has about $1e^-/50$ $Å^2$), where only 3.8% of these amines are charged, we can reasonably conclude that the surfaces have a net negative charge.
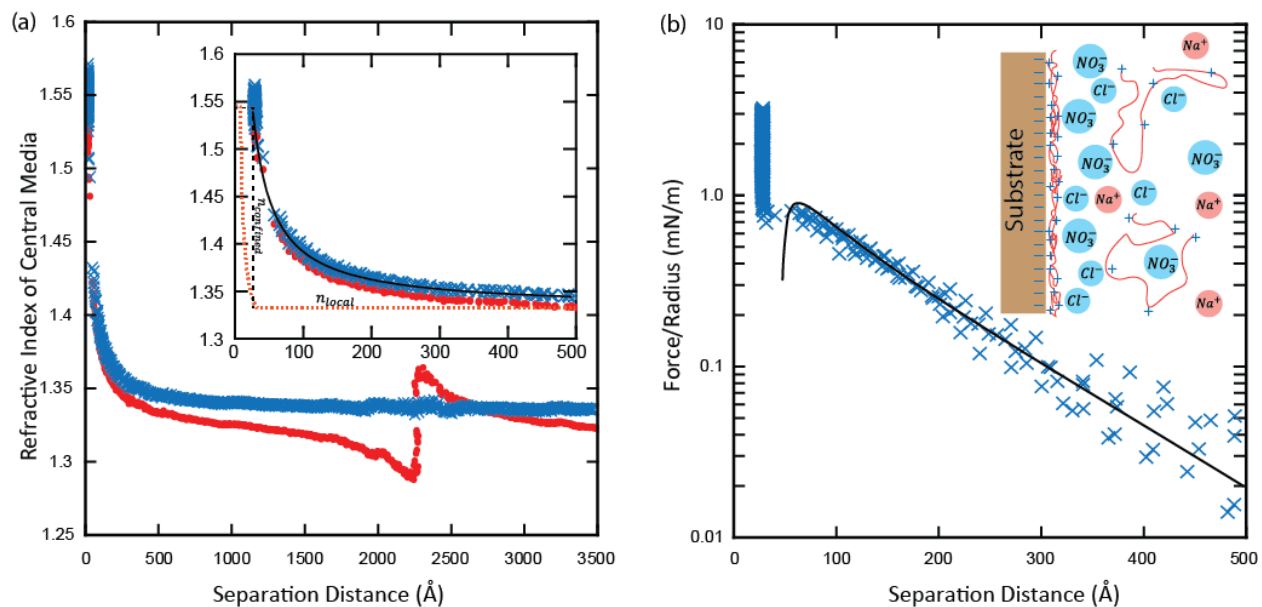

Figure 3.4 (a) Plot of the mean refractive index of the adsorbed PEI film and 0.5 mM NaNO₃ solution before (red circles) and after (blue ×) correcting type 1 and type 3 systematic errors. These corrected profiles represent the weighted average across the central medium including the LPEI layers and electrolyte solution. (Inset) Close-up of refractive index at low separation distances. The dotted line is an illustration of what the corresponding local refractive index may look like at an individual surface with a tightly bound LPEI film. (b) Semi-log plot of the force profile between the surfaces as a function of mica substrate separation with a schematic illustration of the system. The black line is a fit to the data using DLVO theory.

Compared to our earlier work [99] we were able to form a denser layer of LPEI on the mica surfaces by increasing the electrolyte concentration through the presence of Cl⁻ counterions from the LPEI,

compared to a film adsorbed from the same solution but then equilibrated in a polyelectrolyte and Cl-free solution of 0.5 mM NaNO$_3$. The increased electrolyte screened the electrostatic interactions between the chains allowing for a more compact film. While polyelectrolyte films are generally considered to be irreversibly adsorbed, those with lower molecular weight such as the LPEI used here and in the previous experiment (recall that the Cl$^-$ counterion makes up 40-50% of the molecular weight), may partially desorb upon dilution [107]. Thus, the lower adsorbed amount of PEI after equilibration in PEI-free solution is most likely a result of partial desorption.
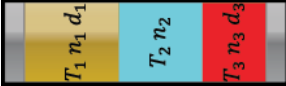
Further extension of RIPC analysis

The extension of the RIPC method to more complicated systems is contingent on the ability to unambiguously specify all but one of the layer properties included in the contact spectrum, prior to the RIPC analysis. If this is possible, then the other steps in the analysis should follow the same two-step approach as those discussed. None of the layer properties need to be known to perform this analysis for asymmetric 3-layer and symmetric 5-layer interferometers. Preliminary tests of more complicated systems were accomplished by simulating contact spectra and finding the conditions where a unique solution could be found. These findings are shown in Table 3.3. Ultimately, with appropriate conditions, three unknown properties (four if any are dispersion coefficients) can be uniquely defined using a single spectrum of an interferometer with multiple layers (only one unknown plus a dispersion coefficient can be defined with a 1 layer interferometer). If the contacting layers have asymmetric thicknesses, their individual thicknesses can be defined using profile measurement as with the 3-layer asymmetric system. Then one global parameter, $\Delta\Omega$, and the corrected refractive index profile can be found from correction of type 1 and type 3 errors.

Under the circumstance of having four unknown properties in the contact spectrum (one being a dispersion coefficient), the minimum number of fringes required for a unique solution is four. However, many more fringes are required to achieve reasonable uncertainty. Consider as an example the 5-layer

system, with the deposited layer thickness and refractive index both varied when fitting the contact spectrum from the previous section. The contact spectrum for this system had twelve fringes and was analyzed with four unknowns during the RIPC analysis, which yielded the high uncertainties given in the last row of Table 3.1. It is estimated that 45 fringes would be required to achieve an uncertainty of less than ± 1 Å at all thicknesses for this system. The uncertainty was also linearly related to the deposited film thickness, with thinner films having substantially greater uncertainty. A 100 Å reduction in the deposited film thickness used in the simulated 5-layer system would triple the uncertainties in the substrate and film properties. Thus, thicker deposited films and more fringes will yield more precise contact properties, while the ΔΩ will be less affected. Furthermore, while the RIPC method is theoretically possible for the systems in Table 3.3, the importance of random error must be assessed for every system, especially when using the maximum number of variables to analyze the contact spectrum.

Several of the systems in Table 3.3 have contacting layers of asymmetric materials. While one of these can be analyzed using the RIPC method without additional known properties (4-layer system with symmetric substrate), this raises additional complications because the refractive index profile might be different at either surface. The detailed effects of having an asymmetric local refractive index profile are beyond the scope of this paper, but we suspect that the ΔΩ at either surface would be additive and could not be determined independently. Therefore the ΔΩ would have to either be known for one of the surfaces by first doing RIPC analysis on a symmetric system, or the effect would need to be much larger at one of the surfaces. Naturally, the RIPC analysis becomes more complicated and error-prone with more complicated interferometers, and the software development can be very time consuming, so it is advantageous to design the interferometer around simpler analysis whenever possible.

Table 3.3 Various interferometry systems that can be analyzed using the RIPC method. Here, d_n refers to the Cauchy dispersion coefficient of the nth layer.

Interferometer system and variables	Interferometer system name	Specified from contact	Additional specifications
	3-layer symmetric	d_1 and one of T_1, n_1	none
	3-layer with asymmetric substrate thickness	T_1^a, T_3^a, d_1	none
	3-layer with asymmetric substrate materials	d_1 and three of T_1, n_1, T_3, n_3, d_3	one of T_1, n_1, T_3, n_3, d_3
	5-layer symmetric	d_1 and three of T_1, n_1, T_2, n_2	none
	5-layer with asymmetric substrate thickness	d_1 and three of T_1, n_1, T_2, n_2, T_4	one of T_1, n_1, T_2, n_2, T_4
	5-layer with asymmetric deposited layer	T_2^a, T_4^a, d_1 and two of T_1, n_1, n_2	none
	4-layer with symmetric substrates	d_1 and three of T_1, n_1, T_2, n_2	none
	5-layer with asymmetric deposited material	d_1 and three of T_1, n_1, T_2, n_2, T_4, n_4	two of T_1, n_1, T_2, n_2, T_4, n_4

[a] Profile data is required to independently define these thicknesses as described for the 3-layer asymmetric system.

Conclusions

The RIPC method has been extended to allow non-contact detection of film or fluid properties near a surface using 5-layer symmetric interferometers and 3-layer asymmetric interferometers with symmetric materials. The approach does not require any *a priori* known properties. Through the application of the RIPC method to realistic simulated data, it has been demonstrated that both systems will return accurate values of all varied properties and will always return precise values of $\Delta\Omega$ for which the method was designed. The technique was applied to a physical system of a PEI film adsorbed to asymmetric mica substrates from an electrolyte solution. A thickness of 15.9 Å and a refractive index of 1.54 was measured without contacting the PEI film. This result is in excellent agreement with the dry film

thickness of 15.8 ± 0.1 Å and refractive index of 1.538 ± 0.007 measured using conventional SFA methods with the films in contact. The LPEI was tightly bound to the surface due to screening of polymer-polymer electrostatic interactions as indicated by a force profile with an attractive Van der Waals minimum and no measurable steric repulsion beyond the hard wall repulsion. Furthermore, it is possible to extend this method to 5-layer systems with deposited layers of asymmetric thickness and symmetric refractive index, or a 4-layer system where the central media is separating a deposited film and the opposite substrate. More complex systems will require some properties to be precisely known for application of the RIPC method to be possible.

Acknowledgement

Chapter IV

Density and Phase State of a Confined Nonpolar Fluid

*Daniel F. Kienle and Tonya L. Kuhl**
Department of Chemical Engineering and Materials Science, University of California Davis, 95616, USA
*Corresponding author. E-mail: tlkuhl@ucdavis.edu

Abstract

Measurements of the mean refractive index of a sphere-like, non-polar fluid, octamethytetracylclosiloxane (OMCTS), confined between mica sheets, demonstrate direct and conclusive experimental evidence of the absence of a first-order liquid to solid phase transition in the fluid when confined. Such a phase transition had been suggested to occur from previous experimental and simulation results on confined nonpolar materials. The results also show that the density remains constant throughout confinement, and that the fluid is incompressible. This along with literature observation of viscosity increases of several orders of magnitude during confinement demonstrate that the molecular motion is limited by the confining wall and not the molecular packing. In addition, the recently developed refractive index profile correction (RIPC) method which enables the structural perturbation inherent at a solid-liquid interface and that of a liquid in confinement to be determined independently, was used to show that there was no measurable excess or depleted mass of OMCTS near the mica surface in bulk films or confined films of only two molecular layers.

Communication

A great amount of work has been devoted to developing an understanding of the behavior of confined fluids, which has proven to be a daunting task. In the literature, there still exist considerable disagreement and conflicting results regarding this subject. Although it is generally agreed upon that a non-polar fluid becomes more solid-like when confined to a thickness below 4-6 molecular layers, [108-115] the molecular interpretation of this phase transition is an area of contention. Two competing theories based on differing experimental results dominate the literature. The experimental observation of first-order confinement-induced freezing is based on the onset of a static friction and a sudden, many orders of magnitude increase in viscosity when the fluid is confined to a particular separation distance [110-112, 114, 116, 117]. Other experiments observed viscoelasitcity in the fluid prior to the onset of a critical shear stress [108, 118, 119] and a continuous transition in the viscosity [109, 120-125], leading to the conclusion that the fluid was approaching a glass transition. It has been suggested that the experimental results supporting either of these theories are fundamentally in agreement and that the conflicting models arise from differences in resolution and interpretation of the results [126]. Contamination from nanoparticles has also been suggested as a cause of discrepancies in the data [77, 127-129], while other research indicates that the role of nanoparticles is unimportant [114, 117]. This is perhaps why the subject remains controversial despite decades of research.

With a small system volume, Lennard-Jones spherelike molecular interactions, and near perfectly flat surfaces, the confinement of non-polar octamethytetracyclosiloxane (OMCTS) between molecularly smooth surfaces seems ideal for computer simulations, and countless studies have been performed. The majority of detailed molecular dynamics simulations have observed crystallization of nonpolar molecular fluids under increasing confinement to 4-6 molecular layers. These findings are summarized in a recent review [130]. However, there are several simulations which indicate that no phase transition occurs until

64

a separation of only two molecular layers, if at all [131-134]. Consequently, simulation studies have not yet conclusively resolved the molecular behavior of confined fluids.

Experimentally, these conflicting theories are both based on shear force measurement between the confining surfaces as opposed to direct measurements of the fluid structure properties, and a conclusive result may only come with direct measurements of the fluid structure. Up to this point, no experimental technique has been capable of directly observing any first order phase transition by structural measurements. The SFA has been used to measure the fluid density (via refractive index) of cyclohexane previously, but the results are difficult to interpret [77, 78], In one case the mica surfaces were likely contaminated with platinum particles [78], and when repeated with particle free surfaces, the results showed unusual time dependent onset of force oscillations, with transitions starting as far out as 120 Å (30 molecular layers); a phenomenon that had not been observed in prior literature, nor has it been repeated since. X-ray reflectivity (XRR) has also been used to determine the fluid density distribution in confinement. The results directly confirm the layered structure of the confined fluids, but could not indicate or refute a first order phased transition [68, 101].

Indeed, the structural and dynamic behavior of a molecularly thin film during confinement, and the effects of compression and tension on the structure, are not well understood primarily due to the inherent difficulty of directly measuring fluid properties at such extremely small length-scales. Using the surface force apparatus and the recently developed RIPC analysis [99], we were able to determine the effects of confinement on the refractive index and thereby density of OMCTS. RIPC analysis sets this experiment apart from previous attempts to measure the refractive index of confined fluids, because the method corrects systematic error that is relevant in almost every experiment and allows for independent determination of the near surface properties of bulk and nano-confined fluids, which have been convoluted in previous measurements of this type [77, 78]. As a result, we can simultaneously quantify any surface excess or depleted mass of OMCTS at a mica surface, any density changes (via refractive index)

that occur when the fluid is confined to a nano-slit, and the corresponding interaction forces during confinement. Thus, we can observe changes in density that would occur with a phase transition.

The muscovite mica substrates used in this experiment were cleaved to sheets with uniform thicknesses of 3-7µm and cut with surgical scissors to avoid the possible influence of platinum particle contamination which has been suggested to occur when the mica is cut with a superheated platinum wire [80, 81]. The mica was then silvered on the back side and glued onto cylindrical BaLF4 glass disks using refractive index matched EPON 1002F epoxy resin. The resulting cylinder radii ranged from 2 to 5 cm. The surfaces were rinsed with water and blown dry with nitrogen to remove any mica particles from the substrates. The disks were then mounted in a cross cylinder orientation in a sealed SFA over P_2O_5. The SFA was purged with dry nitrogen and left for 30 minutes to allow the P_2O_5 to further dry the surfaces before the mica-mica contact measurement was taken. Then, without changing the position of the samples or any optics, the SFA was opened and several drops of 99.6% pure OMCTS (used as received from Sarachem Labs and stored under dry nitrogen with desiccant) were place between the surfaces. The SFA was again sealed and dried as before.

White light was passed normally through the samples to generate optical interference patterns with intensity peaks called fringes of equal chromatic order (FECO) [91]. Spectral images included the FECO and krypton calibration lines (the FECO and calibration lines were on separate portions of the spectral image) such that every data point could be calibrated independently. This is extremely important for sensitive refractive index measurements, where minute thermal drift in the spectrometer can cause unphysical observations in the measured refractive index, especially at low separation distances. The FECO wavelengths were used with the multilayer matrix method [47] to determine uncorrected mica and OMCTS film properties. Using the recently developed RIPC method [99], systematic error that exists in the refractive index-distance profile was corrected to determine accurate substrate properties and to

quantify the optical thickness of any film or bulk density variations at the OMCTS-mica interface prior to, or induced by, confinement.

Force and refractive index-distance profiles were measured by driving the lower surface which was mounted on a spring (K = 260 N/m) at constant step sizes from separation distances of around 3500 Å to contact and determining the spring deflection, which was used to determine the force based on Hook's Law. In total, 36 force-distance profiles from six independent sample sets were measured. Refractive index profiles and RIPC analyses were determined for 19 runs from three sample sets, which were free of optical artifacts that can cause large error in refractive index and small error in separation distance (e.g. external interference from glue layer, particles in camera/spectrometer, large background, etc.). For each sample set, one profile was measured using a combination of mechanical drift and piezoelectric displacement of the top surface to drive the surfaces into contact, without any motor actuation. Prior to experiencing any forces, the samples approached one another at nearly constant speeds of between 2 and 3 Å/s, depending on the sample. Force data was also calculated for these runs based on the assumption that the rate of drift remained constant after the onset of the repulsive solvation forces.

The average force and position acquired for each layer transition across all 36 force runs is shown in Figure 4.1a. The results follow a similar trend and fall within the expected range of forces from the literature [117]. There was no consistent difference in the location, or force of the layer transitions between the motor driven experiments and the mechanical drift driven experiments, thus hydrodynamic effects seem to have had little impact on the forces measured, and the rate of approach did not affect the measured refractive index or calculated density of the fluid.
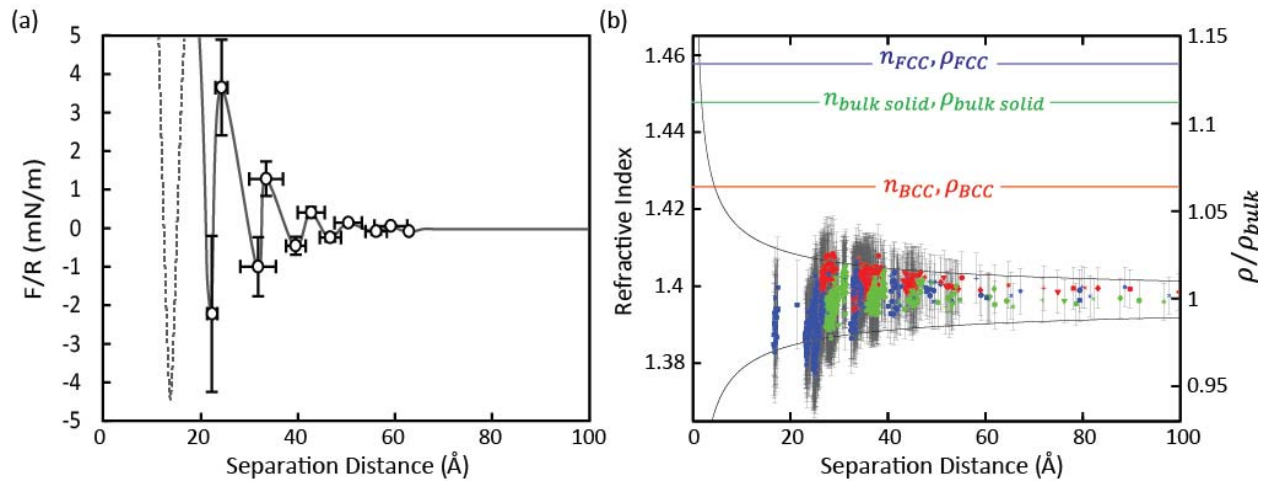
Figure 4.2 (a) Average force and separation distance where layer transitions occurred for all measured force runs. The black line is an illustration of what the full force profile would look like based on the measured forces, and the dashed line is an extrapolation not based on any force measurements. (b) The mean refractive index and normalized density (calculated from the Lorentz-Lorenz equation) of the OMCTS film during confinement is plotted against the separation distance between the surfaces. The different colors represent different samples and the different symbols represent different runs. The error bars are system dependent and were determined using Monte Carlo type error analysis as described previously [92]. The two black lines represent a confidence interval about the bulk properties where data between these lines show no measureable difference from the bulk fluid properties. The red, blue and green horizontal lines are the expected densities and refractive indices of a crystal of Lennard-Jones spheres with body-center-cubic (BCC), face-center-cubic (FCC) lattice structures and the density of crystalline OMCTS [135] respectively.

Importantly, no distinct boundary layer or change in OMCTS density was observed at the mica surface or when confined. At all separations, the change in optical thickness of the fluid relative to bulk was ± 0.1 Å, corresponding to an OMCTS surface excess of ± 0.2 mg/m² (calculated from the Lorentz-Lorenz equation). The uncertainty given is the standard deviation of all runs, and is acceptable for the RIPC method with random error [99]. This result demonstrates that any surface excess or depletion of OMCTS density near the surface is below detection.

The density change corresponding to transition of a fluid of Lennard-Jones spheres in a random close packed configuration to a crystal of Lennard-Jones spheres in hexagonal close pack (i.e. a first-order phase transition) is well above resolution at the separation distance where a phase transition has been suggested to occur (30-60 Å). At these separation distances, the experimental setup had a refractive index

resolution of better than ±0.012,[d] which translates to an OMCTS density resolution of ± 0.03ρ_{bulk}. Thus, a first order phase transition that will increase density by ~0.14ρ_{bulk} would be easily detected.

Figure 4.1b shows the mean refractive index and corresponding density-distance profiles for 19 runs from three samples. As can be seen, the refractive index and density of the fluid remains within resolution of the bulk liquid value throughout confinement, and never approaches the estimated or measured density of crystalline OMCTS [135]. The simplicity of these results is actually quite interesting. While the body of experimental work surrounding confined liquids has at least agreed that there is some type of confinement induced transition to solid-like behavior, the refractive index reported here demonstrates that there is in fact no measurable density change of the confined liquid at all. That is not to say that the film is behaving as a bulk liquid, but it does not show any discrete or continuous average density changes that would be indicative of a phase transition.

Although these results appear to be incongruent with many previous experiments, recall that the evidence indicating a phase change is based on force measurements alone, and that these are the first reliable measurements of OMCTS force and density profiles. In the following paragraphs, we will discuss the implication of these results with regard to previous experimental findings.

Considering only normal force measurements, the absence of solidification in a confined liquid should not be surprising. The average layer transition step size measured was 8.3 ± 1 Å which is consistent with previous findings [96, 109, 111, 117, 121]. This transition step-size is consistently larger than expected for the removal of a single layer of a close packed crystalline solid. An oscillatory force profile is expected for a fluid with density fluctuations near a surface based on simple qualitative description using chemical potential (contact value theorem) or Van der Waals interactions [49], although these do not quantitatively agree with the lack of density change during the compression observed. The consistent

---

[d] This value was calculated using the method for determining random error based on uncertainty in peak fitting parameters as described in ref. 32. The value is dependent on the sample properties and FECO image quality, and we have reported the highest error between all samples used in this study.

observation that only single molecular layers may be squeezed out during a layer transition and that the squeeze-out front propagates in a fluid-like manner is likewise expected for a layered fluid [136]. This would be very surprising behavior for any type of solid which should undergo a brittle or ductile failure. As OMCTS films only behave elastically in that the force-distance curve between each step is reversible, a brittle failure would be expected if the film were solid.

An interesting property of these fluids is the high compressibility of the film prior to undergoing each layer transition. The average compression for all steps for our system is 1.4 ± 0.8 Å which would correspond to a resolvable density change if the fluid were compressible and the mass in the cavity did not change with the decreasing volume. This effect would manifest as an increase in the refractive index between each step, which would exceed the measured refractive indices beyond error bars for almost every data point in Fig 1b. Thus, the film is actually incompressible and some mass must be redistributed laterally during the compression between steps.

When reduced to 2-3 molecular layers there does appear to be systematic deviation from the bulk refractive index, with the latter decreasing as compression is increased. Although these trends are only just resolvable and should not be considered quantitatively, the trend is consistently observed. At such confinement, molecular motion is extremely hindered, and the squeeze out mechanism is likely different than for thicker films. A possible explanation of the observed decrease in refractive index is that the layers dilate as the molecules interpenetrate and spread to move past one another. It may be that such an effect is only observed at this level of confinement because a layer transition would occur before this effect could be observed in thicker films.

In a bulk liquid, an increase in the viscosity would be expected to coincide with an increase in density. Interpretation of the increased viscosity previously observed in confined fluids is less clear. Our density measurements demonstrate that the density of OMCTS does not change under conditions where the viscosity has been observed to increase by many orders of magnitude. Several recent simulation

experiments have demonstrated that an increase in the viscosity and decrease in the diffusivity of a fluid can occur during confinement without corresponding density changes or phase transitions [131-133]. Given that the density and temperature are constant, the reduction in diffusivity can be considered as solely a result of confinement. As the number of molecular layers decreases and the system becomes more 2-dimensional, the configurational entropy and diffusivity of the film decrease while the viscosity increases.   Although the experimental observation of a viscosity change that is not accompanied by a temperature or density change is very unusual, the direct relationship between entropy and the kinetic properties of a bulk or confined fluid is not a new concept [137-139]. Thus, it is reasonable to conclude that the viscosity increase that accompanies confinement is a result of decreasing entropy instead of molecular packing, and that confined OMCTS is approaching a jammed state.

As a confined fluid that may not be in equilibrium, the possible structure of the film will be complexly related to the structures and interactions of both the fluid and the mica surface. A large array of non-bulk-like phase behaviors have been observed for various confined systems and previously reviewed [140]. The measurements presented here may not be able to distinguish between a liquid and possible phase states that exist only in confined films. For example, an amorphous glass or a highly defective crystalline solid may have densities that do not deviate far from the bulk liquid. Likewise, heterogeneous states such as local freezing of the surface or central layers [140], which have been reported from experimental observations, or crystal bridging [141, 142], which has been predicted by molecular dynamics simulation of confined dodecane, may also be relatively close to bulk liquid density. Simulated observation of crystal bridging support full transition to a tetratic crystalline phase at separation distances below six molecular layers, and in this way contrast with our measurements. Nonetheless, the results illustrate that non-equilibrium phase behavior exclusive to confined films may be expected for mica-confined OMCTS, and such states cannot be ruled out based on our measurements alone.

In summary, direct measurements of the refractive index of confined OMCTS has conclusively demonstrated that there is no confinement induced first order phase transition in OMCTS. The film is also found to be incompressible, so that small changes in the confined volume during compression must lead to lateral displacement of the molecules in the film, as evidenced by a constant density during the compression between steps. These results are most consistent with the conclusion that the fluid is approaching a glass transition where confinement is restricting motion, as opposed to motion restriction being the result of increased molecular packing as is the case for supercooled fluids. Whether or not it is appropriate to consider this system to be supercooled is less clear. Previous experimental observations— which suggested that a crystalline state can be achieved at the same temperature under specific experimental circumstances (circumstances possibly related to better control over surface orientation or chemistry, approach rate, or solvent purity)—would suggest that the confined fluid measured here is in a metastable state.

Acknowledgement

Appendices

Supporting Information for Chapter II

Program algorithm for analysis

The algorithm used to analyze interferometry data and correct type 1 and type 3 errors yielding the specific substrate properties and transition layer ΔΩ is shown in Figure A.1.
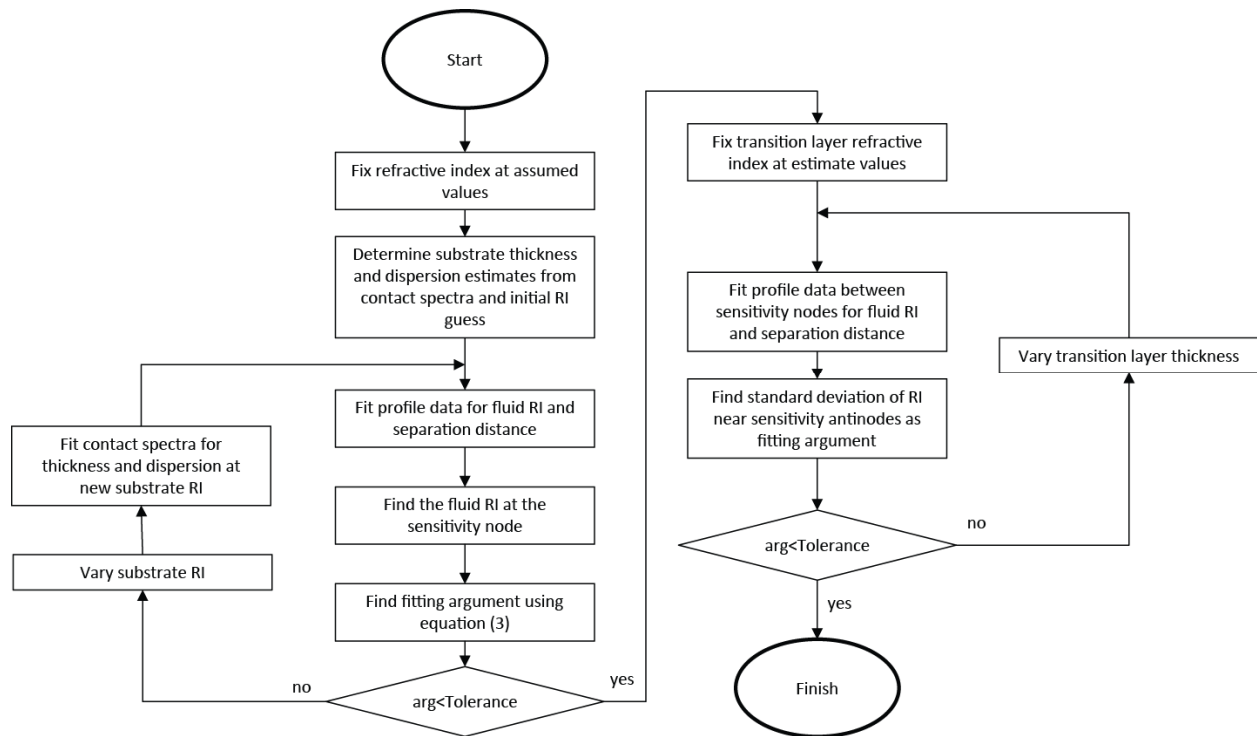

Figure A.1 Schematic of analysis algorithm. Equation 2.3 is referenced in the algorithm (as equations (3)) and is shown below where $n_{node,i}$ is the refractive index at the ith node separation distance, and n_{bulk} is the known bulk refractive index of the fluid.

$$arg = \sum(n_{node,i} - n_{bulk})^2 \qquad (2.3)$$

Analytical method walkthrough
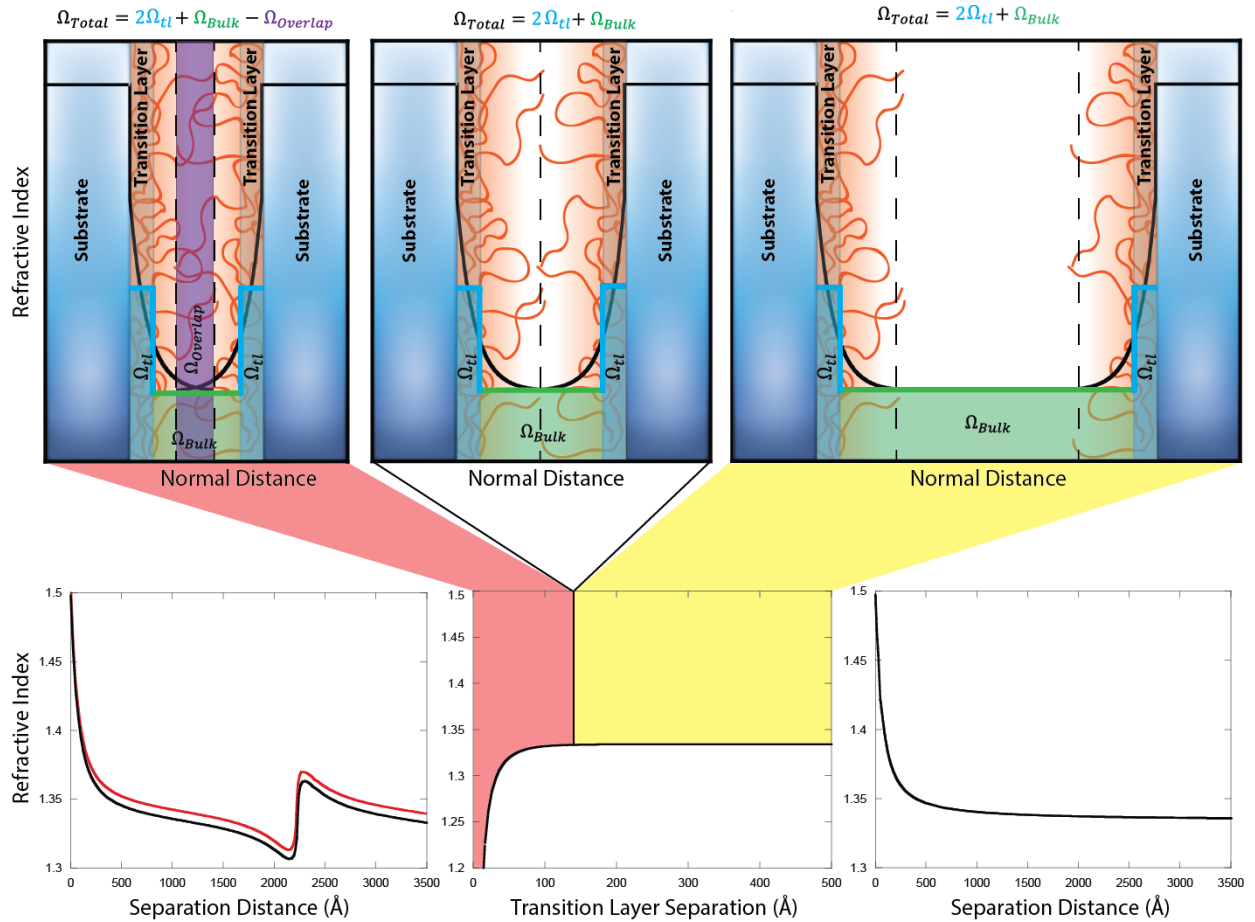
Figure A.2 The top half of the figure illustrates the change in optical thickness for a system where mass is not conserved throughout confinement. The bottom half of the figure shows step-by-step plot of the results after each step of the analysis. All data were generated using the simulation methods described in the paper.

Figure A.2 shows a step by step illustration of the analytical method. The plot in the bottom left shows the first step of the method, applied to refractive index profile data with type 1 and type 3 error (red line) to eliminate the type 1 error, resulting in a system with only type 3 error (black line). After this, the second step of the algorithm was performed on the data to eliminate the type 3 error and determine the $\Delta\Omega$ of the transition layer. The bottom middle plot shows the resulting refractive index profile (n_{fit}) with the transition layers incorporated into the model. Finally, the bottom right plot shows the mean refractive index profile calculated using equation 2.2.

The top half of the figure is an illustration demonstrating why n_{fit} is not at bulk for all separation distances. In each of image, the black line indicates the local refractive index of the central film between the substrates. The blue and green lines illustrate how the system is defined with transition layers to compensate for the variation in the refractive index, where the blue region represents the optical thickness of the transition layer slab (Ω_{tl}) and the green region represent the optical thickness of the bulk layer (Ω_{Bulk}). These regions combined must be equivalent to the total optical thickness of the system which can be taken as the area under the black curve (Ω_{Total}). The yellow region in the n_{fit} plot represents separation distances greater than the overlap separation distance, where the system will look like the top-right and top-middle figures, and Ω_{Total} is accurately described by the combination of the transition layers and bulk slab. The top middle figure represent the overlap separation distance. The red region in the n_{fit} plot represents separations less than the overlap separation distance which is illustrated in the top left figure. Here, the variations from either side are overlapping and the optical thickness of the variations may not be equal to the optical thickness of the transition layers if the profile changes as a result of the overlap. For adsorbed layers, mass of the film should be conserved and the transition layer should accurately represent the overlapping films. If mass is not conserved as illustrated in Figure A.2, the area of the blue and green regions will misestimate the area under the black curve by $\Omega_{overlap}$ which represent the mass lost or gained. Because the Ω_{tl} is fixed, $\Omega_{overlap}$ must be taken from Ω_{bulk} to maintain the total optical thickness of the system, hence the reduction in n_{fit} below the overlap separation distance.

Alternative sources of systematic errors

There are many systematic errors that we know about or have been published about for the SFA in particular, including roughness at silver-mica interface, mismatch between the glue and the disc refractive indices, asymmetry of the interferometer, and unaccounted-for frequency dependence of the refractive index of the central medium. While rarely important, the effects of these errors are occasionally observed. In these circumstances, the perturbations in the refractive index that occur at the sensitivity

antinode cannot be eliminated using the algorithm described because the systematic error has a different effect on the refractive index profile. Results are not used in cases where the systematic error at the sensitivity antinode could not be reduced to below the estimated uncertainty from noise in the analyzed spectra.

An exception to this is the effect of frequency dependence of the central medium, which is typically neglected. This causes a positive or negative peak to appear that is symmetric about the sensitivity antinode. Because the deviation is symmetric, it does not interfere with the correction of type three error, and will be output in the corrected refractive index profile. Typically the height or depth of the peak is below the theoretical resolution estimated based on random error, but the analysis is accurate even if this is not the case.

Supporting Information for Chapter III

Program algorithms for analysis

The algorithms used to analyze interferometry data using the refractive index profile correction (RIPC) method to correct type 1 and type 3 errors yielding the specific substrate and deposited film properties, transition layer $\Delta\Omega$, and corrected refractive index profile for the 3-layer asymmetric (with substrates of identical refractive index), and 5-layer symmetric interferometers are shown in Figure A.3 and Figure A.4 respectively. In these figures, T refers to layer thickness and n refers to layer refractive index and t refers the ratio between the asymmetric substrate thicknesses. The numbered subscripts correspond to the layers in the system as indicated in the interferometer schematic at the top of each figure, and the subscript tl refers to the transition layer. The value of t was found to be independent of the substrate refractive index used to analyze the contact spectrum and is therefore used to calculate the individual substrate thicknesses from the total substrate thickness found from the contact spectrum during analysis of asymmetric 3-layer system.

Figure A.3 Schematic for the RIPC algorithm used to analyze 3-layer asymmetric interferometers. The 3-layer system being analyzed is shown at the top of the figure along with the variables used for this system. For this system T_2 and n_2 are property of the central medium.
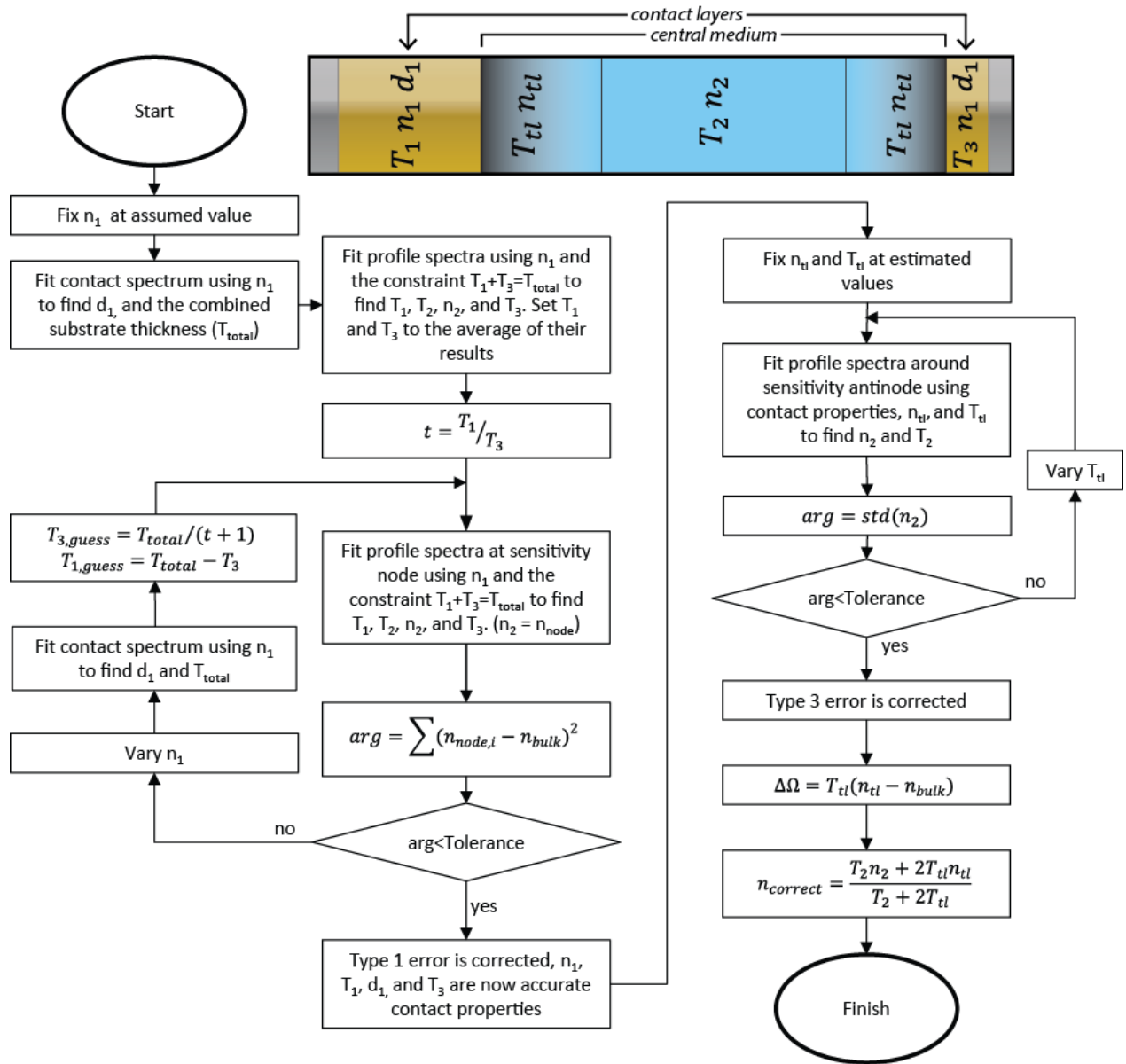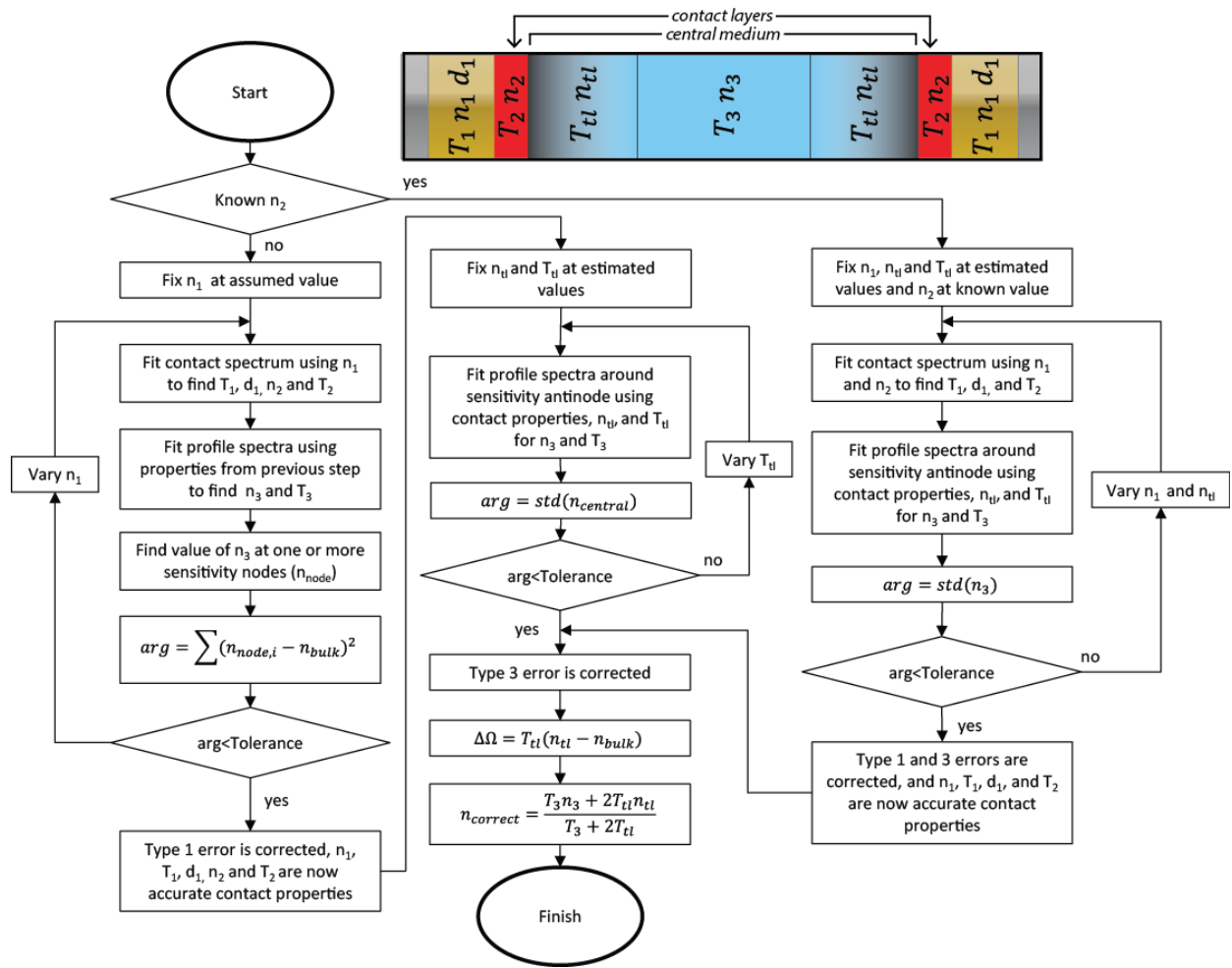
Figure A.4 Schematic for the RIPC algorithm used to analyze 5-layer symmetric interferometers. The 5-layer system being analyzed is shown at the top of the figure along with the variables used for this system. For this system T_2 and n_2 are property of the deposited film and T_3 and n_3 are properties of the central medium.

References

1. Castellana, E.T. and P.S. Cremer, *Solid supported lipid bilayers: From biophysical studies to sensor design.* Surface Science Reports, 2006. **61**(10): p. 429-444.
2. Fischer, A. and E. Sackmann, *Electron-Microscopy and Diffraction Study of Phospholipid Monolayers Transferred from Water to Solid Substrates.* Journal De Physique, 1984. **45**(3): p. 517-527.
3. Hansma, H.G., et al., *Imaging Nanometer Scale Defects in Langmuir-Blodgett-Films with the Atomic Force Microscope.* Langmuir, 1991. **7**(6): p. 1051-1054.
4. Thoma, M., et al., *Ellipsometry and X-ray reflectivity studies on monolayers of phosphatidylethanolamine and phosphatidylcholine in contact with n-dodecane, n-hexadecane, and bicyclohexyl.* Langmuir, 1996. **12**(7): p. 1722-1728.
5. Yang, X.M., et al., *Domain-Structures of Phospholipid Monolayer Langmuir-Blodgett-Films Determined by Atomic-Force Microscopy.* Applied Physics a-Materials Science & Processing, 1994. **59**(2): p. 139-143.
6. Marra, J. and J. Israelachvili, *Direct Measurements of Forces between Phosphatidylcholine and Phosphatidylethanolamine Bilayers in Aqueous-Electrolyte Solutions.* Biochemistry, 1985. **24**(17): p. 4608-4618.
7. Koenig, B.W., H.H. Strey, and K. Gawrisch, *Membrane lateral compressibility determined by NMR and X-ray diffraction: Effect of acyl chain polyunsaturation.* Biophysical Journal, 1997. **73**(4): p. 1954-1966.
8. Arwin, H., *Ellipsometry on thin organic layers of biological interest: characterization and applications.* Thin Solid Films, 2000. **377**: p. 48-56.
9. Richter, R.P. and A.R. Brisson, *Following the formation of supported lipid bilayers on mica: A study combining AFM, QCM-D, and ellipsometry.* Biophysical Journal, 2005. **88**(5): p. 3422-3433.
10. Salamon, Z., et al., *Assembly and Molecular-Organization of Self-Assembled Lipid Bilayers on Solid Substrates Monitored by Surface-Plasmon Resonance Spectroscopy.* Biochimica Et Biophysica Acta-Biomembranes, 1994. **1195**(2): p. 267-275.
11. Toimil, P., et al., *A comparative study of F-DPPC/DPPC mixed monolayers. Influence of subphase temperature on F-DPPC and DPPC monolayers.* Physical Chemistry Chemical Physics, 2010. **12**(40): p. 13323-13332.
12. Steinem, C., et al., *Impedance analysis of supported lipid bilayer membranes: A scrutiny of different preparation techniques.* Biochimica Et Biophysica Acta-Biomembranes, 1996. **1279**(2): p. 169-180.
13. Cherry, R.J. and D. Chapman, *Optical Determination of Thickness of Thin Lipid Films.* Journal of Theoretical Biology, 1969. **24**(2): p. 137-8.
14. Salamon, Z. and G. Tollin, *Optical anisotropy in lipid bilayer membranes: Coupled plasmon-waveguide resonance measurements of molecular orientation, polarizability, and shape.* Biophysical Journal, 2001. **80**(3): p. 1557-1567.
15. Denengelsen, D., *Optical Anisotropy in Ordered Systems of Lipids.* Surface Science, 1976. **56**(1): p. 272-280.
16. Helm, C.A., et al., *Phospholipid Monolayer Density Distribution Perpendicular to the Water-Surface - a Synchrotron X-Ray Reflectivity Study.* Europhysics Letters, 1987. **4**(6): p. 697-703.

17.   Mcintosh, T.J., *Differences in Hydrocarbon Chain Tilt between Hydrated Phosphatidylethanolamine and Phosphatidylcholine Bilayers - Molecular Packing Model.* Biophysical Journal, 1980. **29**(2): p. 237-245.

18.   Nagle, J.F. and S. Tristram-Nagle, *Structure of lipid bilayers.* Biochimica Et Biophysica Acta-Reviews on Biomembranes, 2000. **1469**(3): p. 159-195.

19.   Thoma, M. and H. Mohwald, *Monolayers of Dipalmitoylphosphatidylcholine at the Oil-Water Interface.* Colloids and Surfaces a-Physicochemical and Engineering Aspects, 1995. **95**(2-3): p. 193-200.

20.   Radmacher, M., et al., *From Molecules to Cells - Imaging Soft Samples with the Atomic Force Microscope.* Science, 1992. **257**(5078): p. 1900-1905.

21.   Solletti, J.M., et al., *Characterization of mixed miscible and nonmiscible phospholipid Langmuir-Blodgett films by atomic force microscopy.* Journal of Vacuum Science & Technology B, 1996. **14**(2): p. 1492-1497.

22.   Salamon, Z., H.A. Macleod, and G. Tollin, *Coupled plasmon-waveguide resonators: A new spectroscopic tool for probing proteolipid film structure and properties.* Biophysical Journal, 1997. **73**(5): p. 2791-2797.

23.   Voros, J., et al., *Optical grating coupler biosensors.* Biomaterials, 2002. **23**(17): p. 3699-3710.

24.   Cross, G.H., et al., *The metrics of surface adsorbed small molecules on the Young's fringe dual-slab waveguide interferometer.* Journal of Physics D-Applied Physics, 2004. **37**(1): p. 74-80.

25.   Mashaghi, A., et al., *Optical anisotropy of supported lipid structures probed by waveguide spectroscopy and its application to study of supported lipid bilayer formation kinetics (vol 80, pg 3666, 2008).* Analytical Chemistry, 2008. **80**(13): p. 5276-5276.

26.   Cross, G.H., et al., *A new quantitative optical biosensor for protein characterisation.* Biosensors & Bioelectronics, 2003. **19**(4): p. 383-390.

27.   Swann, M.J., et al., *Dual-polarization interferometry: an analytical technique to measure changes in protein structure in real time, to determine the stoichiometry of binding events, and to differentiate between specific and nonspecific interactions.* Analytical Biochemistry, 2004. **329**(2): p. 190-198.

28.   Salamon, Z., M.I. Brown, and G. Tollin, *Plasmon resonance spectroscopy: probing molecular interactions within membranes.* Trends in Biochemical Sciences, 1999. **24**(6): p. 213-219.

29.   Csucs, G. and J.J. Ramsden, *Formation of planar bilayers from phospholipid vesicles and their interaction with detergents.* Biophysical Journal, 1998. **74**(2): p. A336-A336.

30.   Terry, C.J., et al., *Characterisation of membrane mimetics on a dual polarisation interferometer.* Biosensors & Bioelectronics, 2006. **22**(5): p. 627-632.

31.   Muller, C., P. Machtle, and C.A. Helm, *Enhanced Absorption within a Cavity - a Study of Thin Dye Layers with the Surface Forces Apparatus.* Journal of Physical Chemistry, 1994. **98**(43): p. 11119-11125.

32.   Vigil, G., et al., *Interactions of Silica Surfaces.* Journal of Colloid and Interface Science, 1994. **165**(2): p. 367-385.

33.   Clarkson, M.T., *Multiple-Beam Interferometry with Thin Metal-Films and Unsymmetrical Systems.* Journal of Physics D-Applied Physics, 1989. **22**(4): p. 475-482.

34.   Horn, R.G., D.R. Clarke, and M.T. Clarkson, *Direct Measurement of Surface Forces between Sapphire Crystals in Aqueous-Solutions.* Journal of Materials Research, 1988. **3**(3): p. 413-416.

35.   Briscoe, W.H., et al., *Synchrotron XRR study of soft nanofilms at the mica-water interface.* Soft Matter, 2012. **8**(18): p. 5055-5068.

36.   Israelachvili, J.N., *Thin-Film Studies Using Multiple-Beam Interferometry.* Journal of Colloid and Interface Science, 1973. **44**(2): p. 259-272.

37.   Horn, R.G. and D.T. Smith, *Analytic Solution for the 3-Layer Multiple Beam Interferometer.* Applied Optics, 1991. **30**(1): p. 59-65.

38.   Kekicheff, P. and O. Spalla, *Refractive-Index of Thin Aqueous Films Confined between 2 Hydrophobic Surfaces.* Langmuir, 1994. **10**(5): p. 1584-1591.

39.   Tadmor, R., N.H. Chen, and J.N. Israelachvili, *Thickness and refractive index measurements using multiple beam interference fringes (FECO).* Journal of Colloid and Interface Science, 2003. **264**(2): p. 548-553.

40.   Leckband, D.E., C.A. Helm, and J. Israelachvili, *Role of Calcium in the Adhesion and Fusion of Bilayers.* Biochemistry, 1993. **32**(4): p. 1127-1140.

41.   Miller, C.E., et al., *Grazing incidence diffraction of cadmium arachidate multilayers at the solid-liquid interface.* Zeitschrift Fur Kristallographie, 2005. **220**(12): p. 987-992.

42.   Watkins, E.B., ., *Structure and Orientational Texture of Self-Organizing Lipid Bilayers.* Physical Review Letters, 2009. **102**(23).

43.   Parratt, L.G., *Surface Studies of Solids by Total Reflection of X-Rays.* Physical Review, 1954. **95**(2): p. 359-369.

44.   Nelson, A., *Co-refinement of multiple-contrast neutron/X-ray reflectivity data using MOTOFIT.* Journal of Applied Crystallography, 2006. **39**: p. 273-276.

45.   Rand, R.P., et al., *Variation in Hydration Forces between Neutral Phospholipid-Bilayers - Evidence for Hydration Attraction.* Biochemistry, 1988. **27**(20): p. 7711-7722.

46.   Rand, R.P. and V.A. Parsegian, *Hydration Forces between Phospholipid-Bilayers.* Biochimica Et Biophysica Acta, 1989. **988**(3): p. 351-376.

47.   Born, M. and E. Wolf, *Principles of Optics*. 6 ed. 1980, Oxford: Pergamon.

48.   Johnson, P.B. and R.W. Christy, *Optical Constants of Noble Metals.* Physical Review B, 1972. **6**(12): p. 4370-4379.

49.   Israelachvili, J.N., *Intermolecular and Surface Forces*. 3 ed. 2011, San Diego: Academic Press Inc.

50.   Stelzle, M., G. Weissmuller, and E. Sackmann, *On the Application of Supported Bilayers as Receptive Layers for Biosensors with Electrical Detection.* Journal of Physical Chemistry, 1993. **97**(12): p. 2974-2981.

51.   Birrell, G.B. and O.H. Griffith, *Angle of Tilt and Domain-Structure in Dipalmitoyl Phosphatidylcholine Multilayers.* Archives of Biochemistry and Biophysics, 1976. **172**(2): p. 455-462.

52.   Mcintosh, T.J., *Effect of Cholesterol on Structure of Phosphatidylcholine Bilayers.* Biochimica Et Biophysica Acta, 1978. **513**(1): p. 43-58.

53.   Ducharme, D., et al., *Ellipsometric Study of the Physical States of Phosphatidylcholines at the Air-Water-Interface.* Journal of Physical Chemistry, 1990. **94**(5): p. 1925-1932.

54.   Plant, A.L., *Self-Assembled Phospholipid Alkanethiol Biomimetic Bilayers on Gold.* Langmuir, 1993. **9**(11): p. 2764-2767.

55.   Salamon, Z., et al., *Interaction of phosphatidylserine synthase from E-coli with lipid bilayers: Coupled plasmon-waveguide resonance spectroscopy studies.* Biophysical Journal, 2000. **78**(3): p. 1400-1412.

56.   Bayerl, T.M. and M. Bloom, *Physical-Properties of Single Phospholipid-Bilayers Adsorbed to Micro Glass-Beads - a New Vesicular Model System Studied by H-2-Nuclear Magnetic-Resonance.* Biophysical Journal, 1990. **58**(2): p. 357-362.

57.   Johnson, S.J., et al., *Structure of an Adsorbed Dimyristoylphosphatidylcholine Bilayer Measured with Specular Reflection of Neutrons.* Biophysical Journal, 1991. **59**(2): p. 289-294.

58.   Lee, E.M., et al., *Determination of the Structure of a Surfactant Layer Adsorbed at the Silica Water Interface by Neutron Reflection.* Chemical Physics Letters, 1989. **162**(3): p. 196-202.

59.   Zwang, T.J., et al., *Quantification of the Layer of Hydration of a Supported Lipid Bilayer.* Langmuir, 2010. **26**(7): p. 4598-4601.

60.   Quirk, J.P. and R.M. Pashley, *The Nature of Contact in Measuring the Forces between Muscovite Surfaces.* Journal of Physical Chemistry, 1991. **95**(8): p. 3300-3301.

61.   Chodankar, S., et al., *Density profile of water in nanoslit.* Epl, 2012. **99**(2): p. 26001.

62.   Poynor, A., et al., *How water meets a hydrophobic surface.* Physical Review Letters, 2006. **97**(26).

63.   Chattopadhyay, S., et al., *How Water Meets a Very Hydrophobic Surface.* Physical Review Letters, 2010. **105**(3).

64.   Mezger, M., et al., *High-resolution in situ x-ray study of the hydrophobic gap at the water-octadecyl-trichlorosilane interface.* Proceedings of the National Academy of Sciences of the United States of America, 2006. **103**(49): p. 18401-18404.

65.   Mezger, M., et al., *On the Origin of the Hydrophobic Water Gap: An X-ray Reflectivity and MD Simulation Study.* Journal of the American Chemical Society, 2010. **132**(19): p. 6735-6741.

66.   Mccrackin, F.L., et al., *Measurememt of Thickness and Refractive Index of Very Thin Films and Optical Properties of Surfaces by Ellipsometry.* Journal of Research of the National Bureau of Standards Section a-Physics and Chemistry, 1963. **A 67**(4): p. 363-377.

67.   Russell, T.P., *X-ray and neutron reflectivity for the investigation of polymers.* Material Science Reports, 1990. **5**(4-5): p. 171-271.

68.   Seeck, O.H., et al., *Observation of thickness quantization in liquid films confined to molecular dimension.* Europhysics Letters, 2002. **60**(3): p. 376-382.

69.   Mulder, D.J. and T.L. Kuhl, *Polymer brushes in restricted geometries.* Soft Matter, 2010. **6**(21): p. 5401-5407.

70.   Hamilton, W.A., et al., *Determining the density profile of confined polymer brushes with neutron reflectivity.* Journal of Polymer Science Part B-Polymer Physics, 2004. **42**(17): p. 3290-3301.

71.   Kuhl, T.L., et al., *Neutron confinement cell for investigating complex fluids.* Review of Scientific Instruments, 2001. **72**(3): p. 1715-1720.

72.   Perret, E., et al., *X-ray reflectivity theory for determining the density profile of a liquid under nanometre confinement.* Journal of Synchrotron Radiation, 2010. **17**: p. 465-472.

73.   Chodankar, S., et al., *Density profile of water in nanoslit.* Epl, 2012. **99**(2).

74.   Schmitt, F.J., et al., *Direct surface force and contact angle measurements of an adsorbed polymer with a lower critical solution temperature.* Langmuir, 1998. **14**(10): p. 2838-2845.

75.   Christenson, H.K., *Capillary Condensation in Systems of Immiscible Liquids.* Journal of Colloid and Interface Science, 1985. **104**(1): p. 234-249.

76.   Kohonen, M.M. and H.K. Christenson, *Capillary condensation of water between rinsed mica surfaces.* Langmuir, 2000. **16**(18): p. 7285-7288.

77.   Heuberger, M. and M. Zach, *Nanofluidics: Structural forces, density anomalies, and the pivotal role of nanoparticles.* Langmuir, 2003. **19**(6): p. 1943-1947.

78.   Heuberger, M., M. Zach, and N.D. Spencer, *Density fluctuations under confinement: When is a fluid not a fluid?* Science, 2001. **292**(5518): p. 905-908.

79.   Heuberger, M., *The extended surface forces apparatus. Part I. Fast spectral correlation interferometry.* Review of Scientific Instruments, 2001. **72**(3): p. 1700-1707.

80.   Kohonen, M.M., F.C. Meldrum, and H.K. Christenson, *Particles on melt-cut mica sheets are platinum.* Langmuir, 2003. **19**(3): p. 975-976.

81.   Ohnishi, S., et al., *Presence of particles on melt-cut mica sheets.* Langmuir, 1999. **15**(9): p. 3312-3316.

82.   Frantz, P. and M. Salmeron, *Preparation of mica surfaces for enhanced resolution and cleanliness in the surface forces apparatus.* Tribology Letters, 1998. **5**(2-3): p. 151-153.

83. Israelachvili, J.N. and G.E. Adams, *Measurement of Forces between 2 Mica Surfaces in Aqueous-Electrolyte Solutions in Range 0-100 Nm.* Journal of the Chemical Society-Faraday Transactions I, 1978. **74**: p. 975-1001.

84. Israelachvili, J.N., et al., *Preparing contamination-free mica substrates for surface characterization, force measurements, and imaging.* Langmuir, 2004. **20**(9): p. 3616-3622.

85. Raviv, U. and J. Klein, *Fluidity of bound hydration layers.* Science, 2002. **297**(5586): p. 1540-1543.

86. Raviv, U., P. Laurat, and J. Klein, *Fluidity of water confined to subnanometre films.* Nature, 2001. **413**(6851): p. 51-54.

87. Christenson, H.K. and J.N. Israelachvili, *Growth of Ionic Crystallites on Exposed Surfaces.* Journal of Colloid and Interface Science, 1987. **117**(2): p. 576-577.

88. Benz, M., et al., *Correlation of AFM and SFA measurements concerning the stability of supported lipid bilayers.* Biophysical Journal, 2004. **86**(2): p. 870-879.

89. Helm, C.A. and J.N. Israelachvili, *The Role of the Hydrophobic Force in Bilayer Adhesion and Fusion.* Makromolekulare Chemie-Macromolecular Symposia, 1991. **46**: p. 433-437.

90. Finessi, M., et al., *Charge Reversal of Sulfate Latex Particles by Adsorbed Linear Poly(ethylene imine) Probed by Multiparticle Colloidal Probe Technique.* Journal of Physical Chemistry B, 2011. **115**(29): p. 9098-9105.

91. Israelachvili, J.N., *Thin-Film Studies Using Multiple-Beam Interferometry.* Journal of Colloid and Interface Science, 1973. **44**(2): p. 259-272.

92. Kienle, D., et al., *Thickness and refractive index of DPPC and DPPE monolayers by multiple-beam interferometry.* Analytical and Bioanalytical Chemistry, 2014. **406**(19): p. 4725-4733.

93. Christenson, H.K., *Adhesion and Surface-Energy of Mica in Air and Water.* Journal of Physical Chemistry, 1993. **97**(46): p. 12034-12041.

94. Ostendorf, F., et al., *Evidence for Potassium Carbonate Crystallites on Air-Cleaved Mica Surfaces.* Langmuir, 2009. **25**(18): p. 10764-10767.

95. Christenson, H.K., et al., *Structuring in Liquid Alkanes between Solid-Surfaces - Force Measurements and Mean-Field Theory.* Journal of Chemical Physics, 1987. **87**(3): p. 1834-1841.

96. Horn, R.G. and J.N. Israelachvili, *Direct Measurement of Structural Forces between 2 Surfaces in a Non-Polar Liquid.* Journal of Chemical Physics, 1981. **75**(3): p. 1400-1411.

97. Pashley, R.M. and J.N. Israelachvili, *Molecular Layering of Water in Thin-Films between Mica Surfaces and Its Relation to Hydration Forces.* Journal of Colloid and Interface Science, 1984. **101**(2): p. 511-523.

98. Jacobsson, R., *Light Reflection from Films of Continuously Varying Refractive Index.* Progress in optics, 1966. **5**: p. 247-286.

99. Kienle, D.F. and T.L. Kuhl, *Analyzing Refractive Index Profiles of Confined Fluids by Interferometry.* Analytical Chemistry, 2014. **86**(23): p. 11860-11867.

100. Mante, P.A., et al., *Probing Hydrophilic Interface of Solid/Liquid-Water by Nanoultrasonics.* Scientific Reports, 2014. **4**.

101. Perret, E., et al., *Molecular liquid under nanometre confinement: density profiles underlying oscillatory forces.* J. Phys.: Condens. Matter, 2010. **22**(23): p. 235102.

102. Donaldson, S., et al., *Development of a general interaction potential for hydrophobic and hydrophilic interactions.* Abstracts of Papers of the American Chemical Society, 2013. **246**.

103. Orozco-Alcaraz, R. and T.L. Kuhl, *Interaction Forces between DPPC Bilayers on Glass.* Langmuir, 2013. **29**(1): p. 337-343.

104. Grabbe, A. and R.G. Horn, *Double-Layer and Hydration Forces Measured between Silica Sheets Subjected to Various Surface Treatments.* Journal of Colloid and Interface Science, 1993. **157**(2): p. 375-383.

105. Horn, R.G., D.T. Smith, and W. Haller, *Surface Forces and Viscosity of Water Measured between Silica Sheets.* Chemical Physics Letters, 1989. **162**(4-5): p. 404-408.

106. Ruths, M., et al., *Repulsive forces and relaxation on compression of entangled, polydisperse polystyrene brushes.* Macromolecules, 2000. **33**(10): p. 3860-3870.

107. Hoogeveen, N.G., M.A.C. Stuart, and G.J. Fleer, *Polyelectrolyte adsorption on oxides .2. Reversibility and exchange.* Journal of Colloid and Interface Science, 1996. **182**(1): p. 146-157.

108. Carson, G., H.W. Hu, and S. Granick, *Molecular Tribology of Fluid Lubrication - Shear Thinning.* Tribology Transactions, 1992. **35**(3): p. 405-410.

109. Demirel, A.L. and S. Granick, *Glasslike transition of a confined simple fluid.* Physical Review Letters, 1996. **77**(11): p. 2261-2264.

110. Gee, M.L., et al., *Liquid to Solid-Like Transitions of Molecularly Thin-Films under Shear.* Journal of Chemical Physics, 1990. **93**(3): p. 1895-1906.

111. Klein, J. and E. Kumacheva, *Confinement-Induced Phase-Transitions in Simple Liquids.* Science, 1995. **269**(5225): p. 816-819.

112. Klein, J. and E. Kumacheva, *Simple liquids confined to molecularly thin layers. I. Confinement-induced liquid-to-solid phase transitions.* Journal of Chemical Physics, 1998. **108**(16): p. 6996-7009.

113. Kumacheva, E. and J. Klein, *Simple liquids confined to molecularly thin layers. II. Shear and frictional behavior of solidified films.* Journal of Chemical Physics, 1998. **108**(16): p. 7010-7022.

114. Perkin, S., et al., *Forces between mica surfaces, prepared in different ways, across aqueous and nonaqueous liquids confined to molecularly thin films.* Langmuir, 2006. **22**(14): p. 6142-6152.

115. Vanalsten, J. and S. Granick, *The Origin of Static Friction in Ultrathin Liquid-Films.* Langmuir, 1990. **6**(4): p. 876-880.

116. Mizukami, M., K. Kusakabe, and K. Kurihara, *Shear resonance measurement on structuring of liquids confined between mica surfaces.* Surface and Colloid Science, 2004. **128**: p. 105-108.

117. Israelachvili, J., N. Maeda, and M. Akbulut, *Comment on reassessment of solidification in fluids confined between mica sheets.* Langmuir, 2006. **22**(5): p. 2397-2398.

118. Granick, S., *Motions and Relaxations of Confined Liquids.* Science, 1991. **253**(5026): p. 1374-1379.

119. Hu, H.W., G.A. Carson, and S. Granick, *Relaxation-Time of Confined Liquids under Shear.* Physical Review Letters, 1991. **66**(21): p. 2758-2761.

120. Demirel, A.L. and S. Granick, *Relaxations in molecularly thin liquid films.* Journal of Physics-Condensed Matter, 1996. **8**(47): p. 9537-9539.

121. Bureau, L., *Nonlinear Rheology of a Nanoconfined Simple Fluid.* Physical Review Letters, 2010. **104**(21): p. 218302.

122. Maali, A., et al., *Oscillatory dissipation of a simple confined liquid.* Physical Review Letters, 2006. **96**(8): p. 086105.

123. O'Shea, S.J. and M.E. Welland, *Atomic force microscopy at solid-liquid interfaces.* Langmuir, 1998. **14**(15): p. 4186-4197.

124. Kaggwa, G.B., et al., *Artifact-free dynamic atomic force microscopy reveals monotonic dissipation for a simple confined liquid.* Applied Physics Letters, 2008. **93**(1): p. 011909.

125. Bureau, L. and A. Arvengas, *Drainage of a nanoconfined simple fluid: Rate effects on squeeze-out dynamics.* Physical Review E, 2008. **78**(6): p. 061501.

126. Demirel, A.L. and S. Granick, *Origins of solidification when a simple molecular fluid is confined between two plates.* Journal of Chemical Physics, 2001. **115**(3): p. 1498-1512.

127. Lin, Z.Q. and S. Granick, *Platinum nanoparticles at mica surfaces.* Langmuir, 2003. **19**(17): p. 7061-7070.

128. Zhu, Y. and S. Granick, *Reassessment of solidification in fluids confined between mica sheets.* Langmuir, 2003. **19**(20): p. 8148-8151.

129. Granick, S., et al., *Reply to comment on reassessment of solidification in fluids confined between mica sheets.* Langmuir, 2006. **22**(5): p. 2399-2401.

130. Cummings, P.T., et al., *Phase Transitions in Nanoconfined Fluids: The Evidence from Simulation and Theory.* Aiche Journal, 2010. **56**(4): p. 842-848.

131. Das, A. and J. Chakrabarti, *Dimensional crossover in fluids under nanometer-scale confinement.* Physical Review E, 2012. **85**(5): p. 050601.

132. Matsubara, H., F. Pichierri, and K. Kurihara, *Mechanism of Diffusion Slowdown in Confined Liquids.* Physical Review Letters, 2012. **109**(19): p. 197801.

133. Somers, S.A. and H.T. Davis, *Microscopic Dynamics of Fluids Confined between Smooth and Atomically Structured Solid-Surfaces.* Journal of Chemical Physics, 1992. **96**(7): p. 5389-5407.

134. Xu, R.G. and Y.S. Leng, *Solvation force simulations in atomic force microscopy.* Journal of Chemical Physics, 2014. **140**(21): p. 214702.

135. Hunter, M.J., et al., *Organo-Silicon Polymers - the Cyclic Dimethyl Siloxanes.* Journal of the American Chemical Society, 1946. **68**(4): p. 667-672.

136. Persson, B.N.J. and E. Tosatti, *Layering Transition in Confined Molecular Thin-Films - Nucleation and Growth.* Physical Review B, 1994. **50**(8): p. 5590-5599.

137. Rosenfeld, Y., *Relation between Transport-Coefficients and Internal Entropy of Simple Systems.* Physical Review A, 1977. **15**(6): p. 2545-2549.

138. Mittal, J., J.R. Errington, and T.M. Truskett, *Relationships between self-diffusivity, packing fraction, and excess entropy in simple bulk and confined fluids.* Journal of Physical Chemistry B, 2007. **111**(34): p. 10054-10063.

139. Adam, G. and J.H. Gibbs, *On Temperature Dependence of Cooperative Relaxation Properties in Glass-Forming Liquids.* Journal of Chemical Physics, 1965. **43**(1): p. 139-&.

140. Alba-Simionesco, C., et al., *Effects of confinement on freezing and melting.* Journal of Physics-Condensed Matter, 2006. **18**(6): p. R15-R68.

141. Jabbarzadeh, A., P. Harrowell, and R.I. Tanner, *Crystal bridges, tetratic order, and elusive equilibria: The role of structure in lubrication films.* Journal of Physical Chemistry B, 2007. **111**(39): p. 11354-11365.

142. Jabbarzadeh, A., P. Harrowell, and R.I. Tanner, *Crystal bridge formation marks the transition to rigidity in a thin lubrication film.* Physical Review Letters, 2006. **96**(20): p. 206102.